KeAi
CHINESE ROOTS
GLOBAL IMPACT

Available online at www.keaipublishing.com/en/journals/journal-of-magnesium-and-alloys/

ScienceDirect

Journal of Magnesium and Alloys 13 (2025) 2680–2698

www.elsevier.com/locate/jma

Full Length Article

Interfacial processes of Mg anodes for magnesium-sulfur batteries: An EIS study ☆

Joachim Häcker[a,*], Tobias Rommel[a], Pia Lange[a], Felix Kampmann[b], Jürgen Remmlinger[b], Zhirong Zhao-Karger[c,d], K. Andreas Friedrich[a,e], Maryam Nojabaee[a]

[a] *Institute of Engineering Thermodynamics, German Aerospace Center (DLR), Pfaffenwaldring 38-40, 70569 Stuttgart, Germany*
[b] *Schaeffler Technologies AG & Co. KG, Rintheimer Querallee 2, 76131 Karlsruhe, Germany*
[c] *Helmholtz Institute Ulm (HIU) Electrochemical Energy Storage, Helmholtzstrasse 11, 89081 Ulm, Germany*
[d] *Institute of Nanotechnology (INT), Karlsruhe Institute of Technology (KIT), Hermann-von-Helmholtz Platz 1, D-76344 Eggenstein-Leopoldshafen, Germany*
[e] *Institute of Building Energetics, Thermotechnology and Energy Storage (IGTE), University of Stuttgart, Pfaffenwaldring 6, 70569 Stuttgart, Germany*

Received 11 October 2024; received in revised form 7 March 2025; accepted 3 April 2025
Available online 8 May 2025

Abstract

The development of magnesium batteries strongly relies on the use of a Mg metal anode and its benefits of high volumetric capacity, reduction potential, low cost and improved safety, however, to date, it still lacks sufficient cycling stability and reversibility. Along with the electrolyte selection, the interfacial processes can be affected by the anode itself applying electrode engineering strategies. In this study, six different Mg anode approaches – namely bare Mg metal, Mg foil with an organic and inorganic artificial solid electrolyte interphase, Mg alloy, Mg pellet and a tape-casted Mg slurry – are selected to be investigated by means of electrochemical impedance spectroscopy in Mg|Mg and Mg|S cells. While a plating/stripping overpotential asymmetry was observed and assigned to the desolvation during Mg plating, the impedance spectra of stripping and plating hardly differ for all applied anodes. In contrast, the sulfur species significantly influence the impedance response by altering the surface layer composition. By systematic process assignment of the gained spectra in Mg|Mg and Mg|S cells, specific equivalent circuit models for different anodes and cell conditions are derived. Overall, the study aims to give valuable insights into the interfacial processes of Mg anodes to support their further development toward long-lasting Mg batteries.

Keywords: Magnesium anode; Artificial solid electrolyte interphase; Electrochemical impedance spectroscopy; Equivalent circuit model; Magnesium-sulfur battery.

1. Introduction

Since decades, it has been attempted to realize a long-lasting lithium metal battery to replace common graphite as anode material and significantly increase the energy density. However, the high reduction potential of Li metal and its tendency to form dendrites result in on-going electrolyte decomposition and potential safety hazard, respectively, and so far, hinders Li metal to be applied as anode in commercial batteries. Thus, other non-noble metals are attracting research interest as alternative metal anodes. Among them, magnesium is a promising candidate due to its volumetric capacity of 3837 mAh cm^{-3}, low tendency for dendrite formation and moderate reduction potential of −2.37 V. Despite latter compromising the energy density, it also offers advantages in terms of processability under ambient atmosphere [1] due to its alleviated reaction with oxygen and moisture compared to lithium metal. In combination with sulfur as cathode active material (gravimetric capacity of 1675 mAh g^{-1}) in a Mg-S cell, an appealing realistic energy density of approx. 250 Wh kg^{-1} results [2]— with advantages in terms of costs, safety and sustainability over LIB. While in the early research stage, the cyclability, i.e. reversible Mg stripping and plating, was limited by the lack of a suitable electrolyte, especially the

☆ Peer review under responsibility of Chongqing University.
* Corresponding author.
E-mail address: joachim.haecker@dlr.de (J. Häcker).

https://doi.org/10.1016/j.jma.2025.04.001

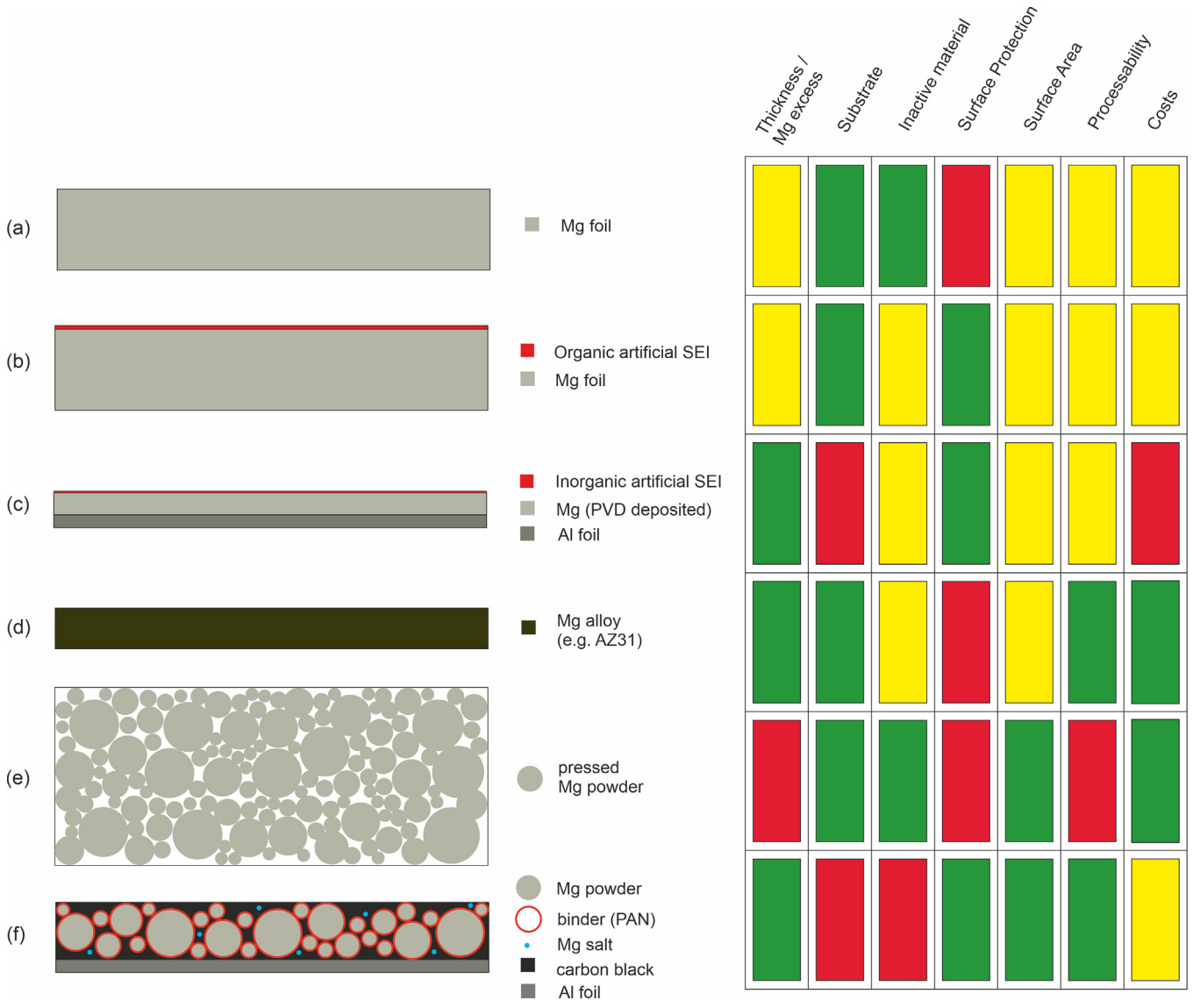

Fig. 1. The six different magnesium anode concepts investigated in this study and their rating in terms of key properties.Thickness not to scale, green to red: advantageous to disadvantageous. (For interpretation of the references to colour in this figure legend, the reader is referred to the web version of this article.)

development of the $Mg[B(hfip)_4]_2$ electrolyte system [3,4], allowed to take further steps toward the realization of a Mg metal anode—and consequently Mg batteries. Along with improvements of the electrolyte composition in regard of solvent choice [5-11] and SEI-forming additives [12-17], the anode itself can be modified [18]. This is indeed a crucial engineering step to enable Mg-based batteries, but attention has to be paid to not diminish the energy density of the final Mg battery by large additional mass or volume of inactive material (i.e. low specific and volumetric capacity), or an altered anode potential.

On first sight, pure Mg metal (Fig. 1a) is the ideal choice as no substrate or other inactive material is needed, i.e. the capacity and reduction potential are not diminished, resulting in a high cell voltage and energy density. However, the bare Mg surface is prone to (repetitively) react with electrolyte species or dissolved cathode active material (e.g. polysulfides) [19] to form an SEI, which does not exhibit desired properties in terms of ionic conductivity and mechanical flexibility. Therefore, a protective surface coating is reasonable to function as an artificial SEI. In case of an organic coating [1,20,21], the polymeric network additionally offers elasticity to withstand volume changes during cycling—at least to some extent (Fig. 1b).

To date, large Mg excess is still essential as current Mg cells are lacking sufficient reversibility with Coulombic efficiencies only reaching 95–99%. However, to realize Mg batteries with competitive energy density to LIB, the anode thickness has to be adjustable to minimize excess Mg while matching the active material content on the cathode side. For example, in case of a sulfur cathode with a practical sulfur loading of 3 mg cm^{-2}, which theoretically equals 5 mAh

cm^{-2}, a perfectly balanced foil anode with no Mg excess would be approx. 13 μm or 26 μm thick for a single or multilayer cell, respectively (assuming the theoretic volumetric capacity of 3833 mAh cm^{-3}). Note, that a thin substrate has to remain after discharge for subsequent plating – thus, little Mg excess is necessary to avoid an additional thin current collector. Due to its lack of ductility, Mg foil can hardly be processed to such low thicknesses with commercially available Mg foils (e.g. by Gelon) only exhibiting a minimum thickness of 100 μm. Lately, Mandai et al. successfully prepared thin Mg foils (40–50 μm) by an extrusion and rolling procedure at 300 °C to result in grain refinement and activation of basal planes necessary for plastic deformation [22]. An even lower and tailored thickness can be achieved by PVD methods like sputtering with the possibility to introduce an inorganic top layer as artificial SEI—e.g. as separate [23-26] or alloying [27,28], phase—in continuation to the Mg active material deposition (Fig. 1c). However, the need of a substrate (e.g. Al foil, < 10 μm) and the time-consuming and costly processing are hurdles for an industrial transfer.

Another option to achieve thin anodes is the application of ductile Mg alloys—on the expense of diminishing the capacity and reduction potential. Among the various alloys being investigated in recent years [29–35], AZ31 (Fig. 1d) appears to be most promising as it only contains 4 wt.% inactive elements (3 wt.% Al, 1 wt.% Zn), offers a comparable cell voltage and can be cold welded to thicknesses below 30 μm [36]. Furthermore, its processing is established and cost-effective due to the use of AZ31 as light-weight alloy in automotive industry.

An alternative possibility to alter the electrochemical processes at the anode/electrolyte interface, i.e. electrolyte decomposition and inhomogeneous Mg stripping/plating [37], is the reduction of the current density by increasing the anode surface area [38]. This is can be achieved by applying Mg powder—either as a pressed 3D powder pellet [39] (Fig. 1e) or tape casted on a substrate [40] (Fig. 1f). Yet, pellets are cost-effective, but hardly scalable and rather thick (hundreds of microns). Both drawbacks can be ruled out by latter tape-casting approach combing scalable processing and potential protective coating, but requires a substrate and lacks electrode density and consequently energy density.

Despite the cited publications already providing valuable insights, an in-depth comparison of the above-named anode approaches is missing. Therefore, this study aims to give insights into the interfacial processes of different Mg anode concepts applying electrochemical impedance spectroscopy (EIS) towards the development of an improved anode concept. While the systematic process identification and assignment were conducted in symmetrical Mg|Mg cells, the practical performance during charge and discharge was investigated in Mg|S cells. It was found, that two main interfacial processes are present at the Mg anode, which could be assigned to the charge transfer and diffusion through the SEI layer. By introducing an organic artificial SEI, the porous coating morphology becomes obvious in the ultrahigh frequency region of the impedance response. In case of extended OCV conditions a high-ohmic adsorption layer is reversibly forming, which is less pronounced in presence of sulfur species in Mg|S cells. In general, significant differences arise comparing full cells to symmetrical cells. The anode impedance not only exhibits higher overall resistances in Mg|S cells, specifically the Mg plating is affected by sulfur species in the electrolyte as low-frequency inductive loops appear at the beginning of charge, which can be clearly assigned to a Mg surface effect, most likely Mg^{+} surface relaxation. Additionally, the charge transfer kinetics are retarded in the presence of sulfur species. Finally, equivalent circuit models (ECM) are derived and discussed. Despite the results being evaluated in the context of Mg-sulfur cells, the findings might be applicable to magnesium batteries in general – yet with other specific surface reactions due to different electrolytes. For example, in aqueous Mg-air batteries the Mg alloy morphology, e.g. the grain size and orientation, as well as the surface layer formation ($Mg(OH)_2$ herein) were found crucial for the battery performance [41]. Similar impedance spectra and ECM result, wherein inductive loops are related to corrosion processes [42].

2. Experimental

2.1. Mg anode preparation

Different magnesium anode concepts are investigated, wherein Mg foil (Gelon, 100 μm) serves as benchmark material. After cutting into 18 mm disks, it was scraped before cell assembly inside the Ar-filled glovebox to remove the native oxide layer.

The organic artificial SEI was prepared following our previous study [1]. In brief, Aquivion and PVDF solution were mixed in 1:1 vol. ratio and spin coated on a freshly scraped Mg foil under ambient atmosphere. It was dried at RT with an additional drying under vacuum before cell assembly. The thickness has a radial gradient of > 0.5 μm in center and > 1 μm at the edges.

The Mg anode with an inorganic artificial SEI was prepared by sputtering Mg (approx. 20 μm) on an Al substrate (12 μm). Subsequently, an inorganic a-SEI (approx. 100 nm) was introduced by reactive sputtering.

AZ31 (96/3/1 wt.% Mg/Al/Zn) was selected as magnesium alloy due to its low number of alloying elements and its ductility. By extensive rolling of AZ31 sheets, a thickness as low as 30 μm was achieved.

Mg pellets were prepared by pressing Mg powder (Alfa Aesar, 325 mesh, 99%) in a customized press die with 18 mm diameter under Ar atmosphere to result in 600–800 μm thick anodes. No additional scraping was done before cell assembly.

The Mg wet coating followed the preparation route of Son et al [40]. In brief, Mg powder, carbon black, Mg triflate and poly(acrylonitrile) (PAN) were dispersed in DMSO in 80:10:5:5 ratio and coated on C-coated Al foil (22 μm) inside an Ar-filled glovebox applying tape casting. The coating was dried at 100 °C under vacuum with a subsequent 1 h step

at 250 °C to induce the ring polymerization of PAN. The thickness varies in the range of 30–40 μm.

Ring-shaped reference electrodes were manufactured by either die cutting Mg foil (Gelon, 100 μm) or pressing Mg powder (Alfa Aesar, 325 mesh, 99%) in a customized press die with 19 and 21.5 mm inner and outer diameter—tailored for the use in the ECC-PAT-Core cells.

2.2. Electrolyte and sulfur cathode preparation

Magnesium hexafluoroisopropyloxy borate ($Mg[B(hfip)_4]_2$) was synthesized and dried as depicted in previous studies [4]. A 0.2 M electrolyte was prepared by dissolving 1 mmol $Mg[B(hfip)_4]_2$ in 5 mL dimethoxyethane (G1, monoglyme, 99.5 %, < 10 ppm H_2O, Acros Organics), vigorous stirring over night and subsequent filtration to remove the trace insoluble residues with a PTFE syringe filter.

For the Mg|S cell investigation, a sulfur composite cathode was prepared with the detailed preparation being indicated in previous studies [43]. In brief, a mechanical intrusion of sulfur into carbon was achieved by ball-milling of sulfur (99.5%, Alfa Aesar) and Ketjenblack EC 600-JD (Akzo Nobel) at 500 rpm for 15 min in a mass ratio of 5:4. A homogeneous slurry was gained by stirring the S-C powder in aqueous carboxymethyl cellulose solution (3.7 wt.% CMC, Walocel CRT 2000 PA, Dow Wolff) and styrene-butadiene rubber solution (40.4 wt.% SBR, JSR TRD 102A, JSR Micro). Subsequently, the slurry was tape casted on C-primed aluminum foil (22 μm) to result in a cathode with 50/40/10 wt.% S/KB/CMC-SBR (CMC:SBR 1:2) and approx. 1.0 $mg_{(S)}$ cm^{-2}.

2.3. Cell assembly and characterization

The polarization and EIS measurements are performed in ECC PAT-Core cells (El-Cell) assembled under Ar atmosphere (O_2 < 1 ppm, H_2O < 3 ppm) applying a magnesium metal reference ring, two separator layers of glass fiber (GF/C, Whatman), 18 mm electrodes and 200 μl 0.2 M $Mg[B(hfip)_4]_2$ / G1 electrolyte.

The test protocol used for the investigation of Mg|Mg cells was established in a previous study [1]. After an initial 50 h OCV phase, polarization cycles at different current densities (0.1–1.0 mA cm^{-2}) with intermittent 10 h OCV were performed. Potentiostatic EIS ("static EIS") and galvanostatic EIS ("dynamic EIS", $I_{EIS} = I_{pol}$) with 5 mV amplitude in a frequency range of 100 mHz to 300 kHz was executed during OCV and polarization, respectively, applying a ZENNIUM and IM6 potentiostat (Zahner).

After an initial 1 h OCV, cycling of Mg|S cells was done at C/10 rate (167.5 mA/$g_{(S)}$) and 25 °C in a voltage range of 0.05 – 3 V. Anode EIS spectra were collected vs. Mg reference electrode every 30 min with constant current density of 0.1 mA cm^{-2} and an amplitude of 5 mV. Thus, the high-ohmic adsorption layer, which forms during relaxation at open-circuit conditions [44] is mitigated and the actual impedance response during operating condition is estimated.

3. Results and discussion

3.1. Mg anode concepts

As illustrated above (Fig. 1), six Mg anode concepts with different benefits were selected for this EIS study, namely: Mg foil—with bare surface and an organic a-SEI coating (Aquivion/PVDF), PVD-deposited Mg with an inorganic a-SEI top layer, Mg alloy (AZ31), pressed Mg pellet and a tape casted Mg slurry. Anode approaches that seem appealing in terms of cycle life [45], but offer a significantly lower capacity and/or redox potential are not considered herein. The surface morphology and composition of the selected anodes are depicted in Fig. 2 and supplementary Figure/Table S1, respectively. The lowest oxygen content (approx. 1 wt.%) was observed in case of PVD-deposited Mg (c) and scraped Mg alloy (d), while the scraped Mg foil (a) exhibits > 3 wt.% O. Such native oxide layer might eventually be beneficial to hinder electrolyte and also sulfur species in Mg-S cells to be reduced at the anode surface [1]—at least initially as this layer will most likely crack upon stripping/plating. Same holds for the Mg pellet (O = 3–5 wt.%) and slurry approach (Fig. 2e,f) as the commercial Mg powder is most likely already oxidized during industrial processing and transport—despite inert atmosphere. Thus, the intuitively high surface will only be partially active. Note, that for all anode concepts still the projected electrode area of 2.545 cm^2 was used for defining the current density during polarization as well as for plotting impedances and resistances.

3.2. OCV and polarization of Mg|Mg cells

The six above-named anode approaches are investigated in a polarization sequence including different current densities (0.1, 0.2, 0.5, 1.0 and concluding 0.1 mA cm^{-2}) as well as initial (50 h) and intermittent OCV phases (10 h). The potentials vs. Mg ring reference electrode during the initial test sequence are depicted in Fig. 3.

As already observed in a previous study [1], all cells initially feature potential instabilities during 50 h OCV (Fig. 3b) probably due to surface conditioning, which vanishes after 10 polarization cycles at 0.1 mA cm^{-2} (Fig. 3c) indicating an established surface layer composition. Upon initial polarization after OCV, an ultrafast (< 1 s) voltage spike of nearly 4 V appears for some cells, which reflects a surface passivation by adsorbed electrolyte species, which desorb under applied bias (see subsequent LF process assignment). The arising overpotential in the 10^{th} polarization cycle of each current density is indicated in Fig. 4 for stripping (a) and plating (b). As expected, the overpotentials linearly increase with increasing current density, with the Mg plating showing higher overall overpotentials than Mg stripping which results in a plating/stripping asymmetry (c), backing our previous study [9]. Generally, the stripping overpotentials show a steeper increase with current than Mg plating—consequently, the plating/stripping asymmetry becomes less significant at higher currents (Fig. 4c, 1.0 mA cm^{-2}). The Mg foil with organic

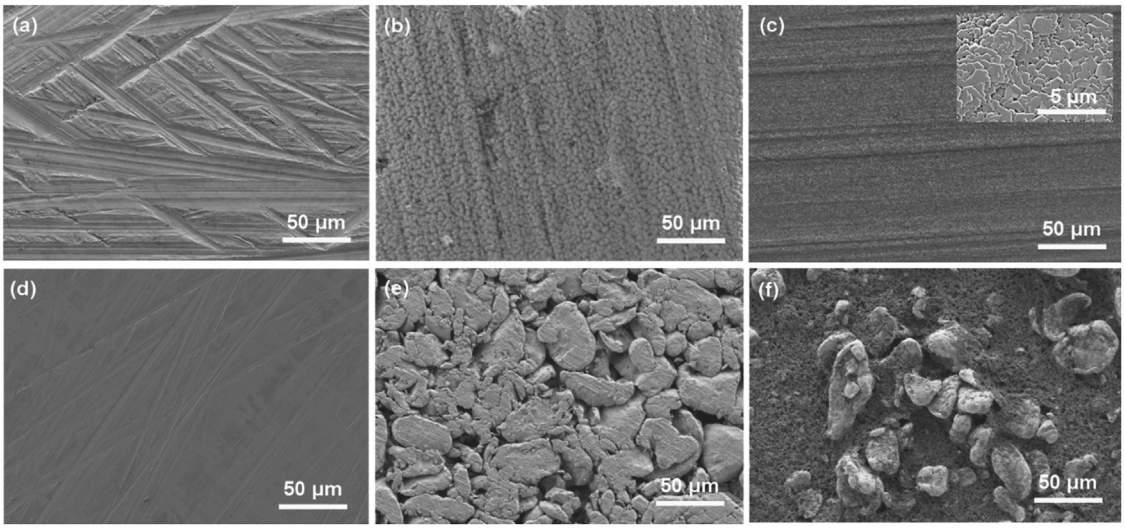

Fig. 2. SEM images of the applied Mg anodes: (a) Mg foil, (b) Mg + organic a-SEI, (c) Mg + inorganic a-SEI, (d) Mg alloy (AZ31), (e) Mg pellet and (f) Mg slurry.

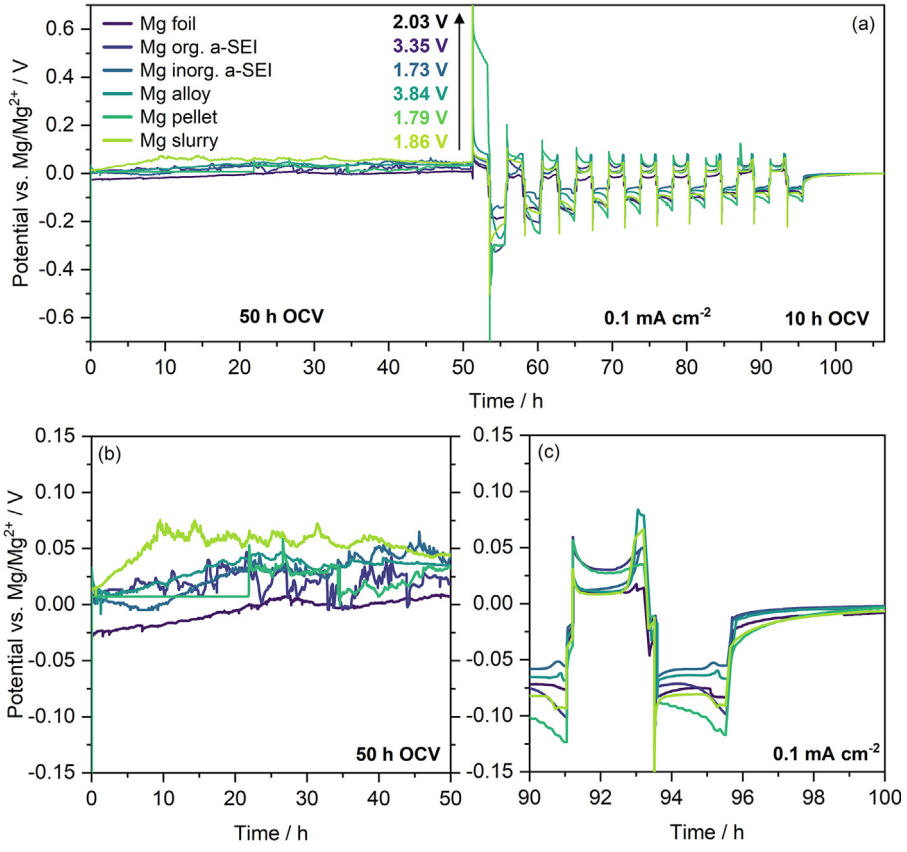

Fig. 3. (a) Polarization procedure with initial (b) 50 h OCV after cell assembly and (c) subsequent polarization at 0.1 mA cm^{-2} with concluding 10 h OCV.

a-SEI, exhibits the highest overpotentials for both stripping and plating, while both organic and inorganic a-SEI anode feature the lowest plating-stripping asymmetry. This reflects the influence of an a-SEI to beneficially alter the interfacial processes in terms of Mg plating (i.e. Mg^{2+} desolvation) [9], but also induces an additional ion diffusion barrier.

3.3. EIS analysis of Mg|Mg cells

3.3.1. Process in the LF region (< 10 Hz)

To gain deeper insights, EIS of the Mg anode (vs. RE) was applied during polarization and OCV phases of Mg|Mg cells. As named above, independent from the applied elec-

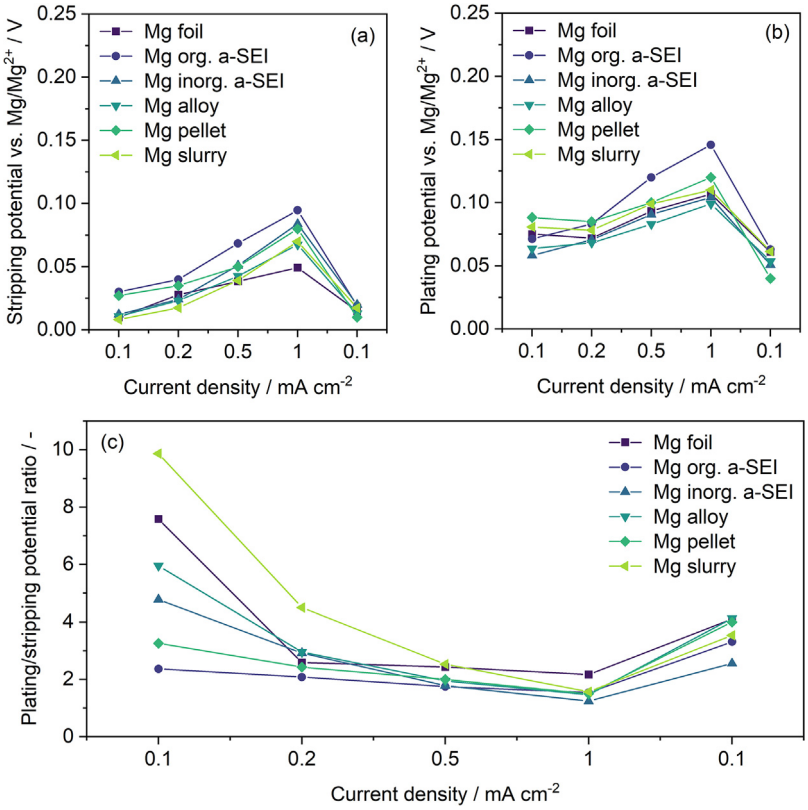

Fig. 4. (a) Stripping and (b) plating potential vs. Mg|Mg^{2+} for all anode approaches during the final cycle of each polarization interval. (c) Current-dependent asymmetry in the plating and stripping potential.

trolyte, magnesium cells exhibit a high voltage spike after extended non-current conditions (OCV) [1,4,44,46] originated in the surface passivation with an adsorption layer, i.e. adsorbed electrolyte salt and solvent molecules [47]. This becomes obvious in the impedance measurements during 50 h OCV ("static EIS", Fig. 5, left column) with an evolving high-ohmic surface resistance (several hundred kΩ) [44] in the low frequency (LF) domain and a peak shifting of the phase angle to lower frequencies indicating a lower time constant.

Interestingly, this phenomenon appears in all anode approaches independent of a surface protection with an a-SEI or bare Mg surface. Indeed, in case of the organic a-SEI, it is plausible that the electrolyte species are in contact with the Mg surface due to the porous nature of the film [1]. In comparison, the Mg alloy exhibits the highest impedance, and consequently highest voltage spike of 3.84 V (Fig. 3), reflecting a preferred adsorption of electrolyte species and complete surface coverage.

When applying a polarization current the adsorbed molecules instantly desorb. By maintaining the current during impedance measurements ("dynamic EIS", Fig. 5, middle column), the electrolyte species stay desorbed and a low-ohmic Mg surface contribution becomes apparent. While being partially superimposed by the adsorption layer during the initial 50 h OCV and a differentiation of the processes is difficult, they become rather distinct in the MF and HF region upon applied current. This points to changes in surface composition and/or morphology during the initial stripping and plating. Not only the processes become distinguishable, they also exhibit a smaller impedance with decreased phase angle compared to the OCV phase indicating the breakage/removal of a native passivating layer with simultaneous formation of an in situ SEI layer and potentially an increase in surface roughness, respectively. Surprisingly, the impedance spectra do not correspond to the plating/stripping asymmetry which indicates the higher overpotential for Mg plating to be caused by a rate-limiting step in the electrolyte, which does not contribute to the anode impedance in that frequency range, rather than an interfacial process. This assumption is backed by a previous theoretical study identifying the desolvation of the Mg^{2+} ion from the monoglyme molecule to be the rate-determining step during Mg deposition [9]. However, the plating features a splitting of the MF process and shift to lower frequencies compared to the stripping process (Fig. 5, middle column), indicating the superposition of two processes.

Importantly, the 10 h OCV period after polarization (Fig. 5, right column) again causes an increase in impedance accompanied with a small voltage spike when subsequently applying a current (Fig. S2). This reversible increase in impedance upon relaxation is yet another indication of adsorption layer formation. However, the formation of such layer appears to be less pronounced most likely due to the formation of an SEI upon polarization. This repeats in subsequent polarization

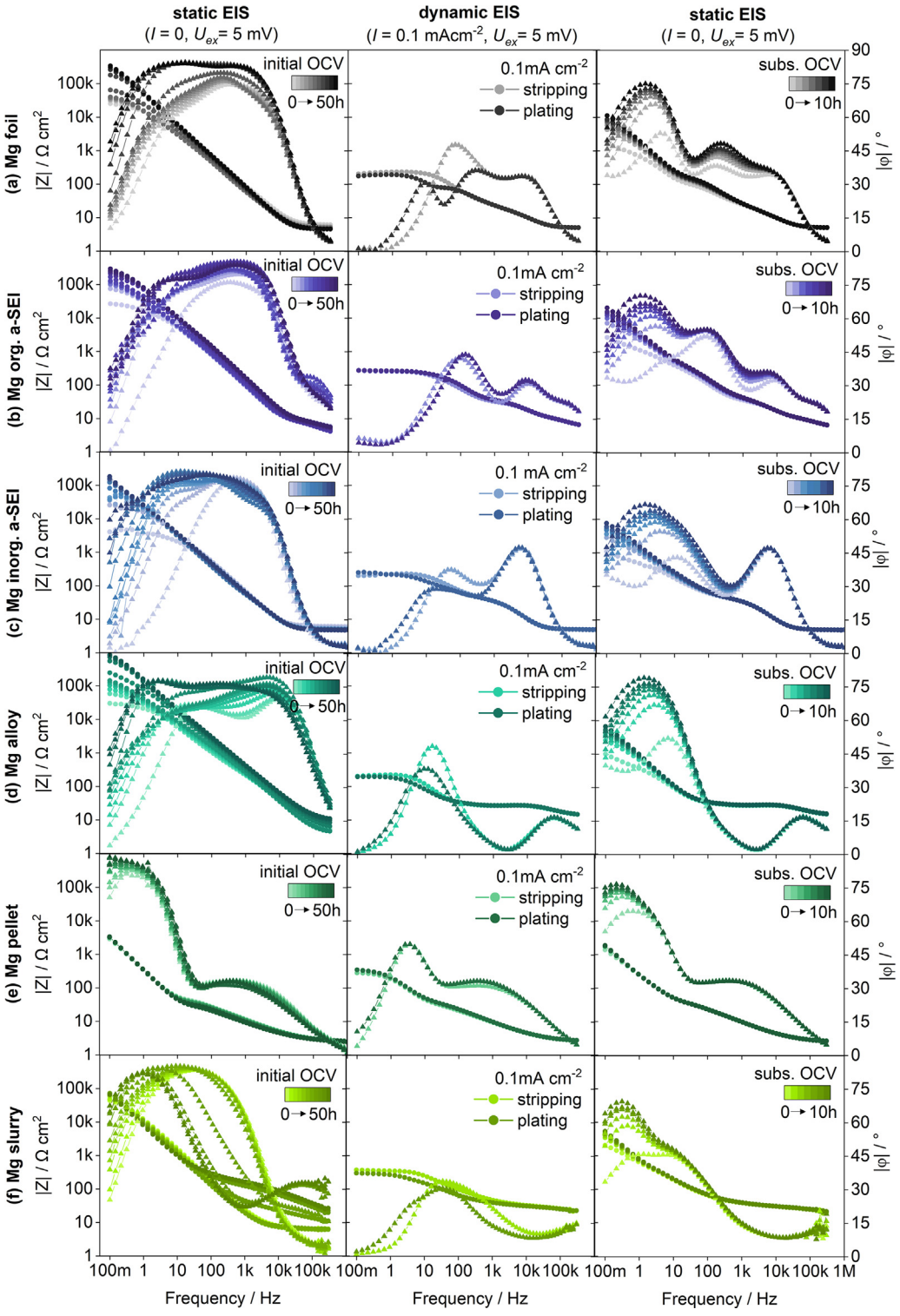

Fig. 5. Bode plots of impedance spectra measured in Mg|Mg cells with different Mg anodes during initial 50 h OCV, stripping and plating at 0.1 mA cm^{-2} (spectra from concluding 10th cycle) and subsequent 10 h OCV. ● |Z| (left axis), ▲ |φ| (right axis). For a reliable EIS analysis reflecting practical resistances, dynamic EIS conditions (applied bias) are crucial. (For interpretation of the references to colour in this figure legend, the reader is referred to the web version of this article.)

cycles with the voltage spike being current-dependent (Fig. S2). Therein, again the organic a-SEI coated Mg exhibits the highest overpotential, i.e. surface coverage. As the adsorption layer is irrelevant for the practical operation of Mg batteries, the following discussion and equivalent circuit model (ECM) development focuses on the galvanostatic ("dynamic" or "operando") EIS during stripping and plating whereby the formation of such adsorption layer, which superimposes the

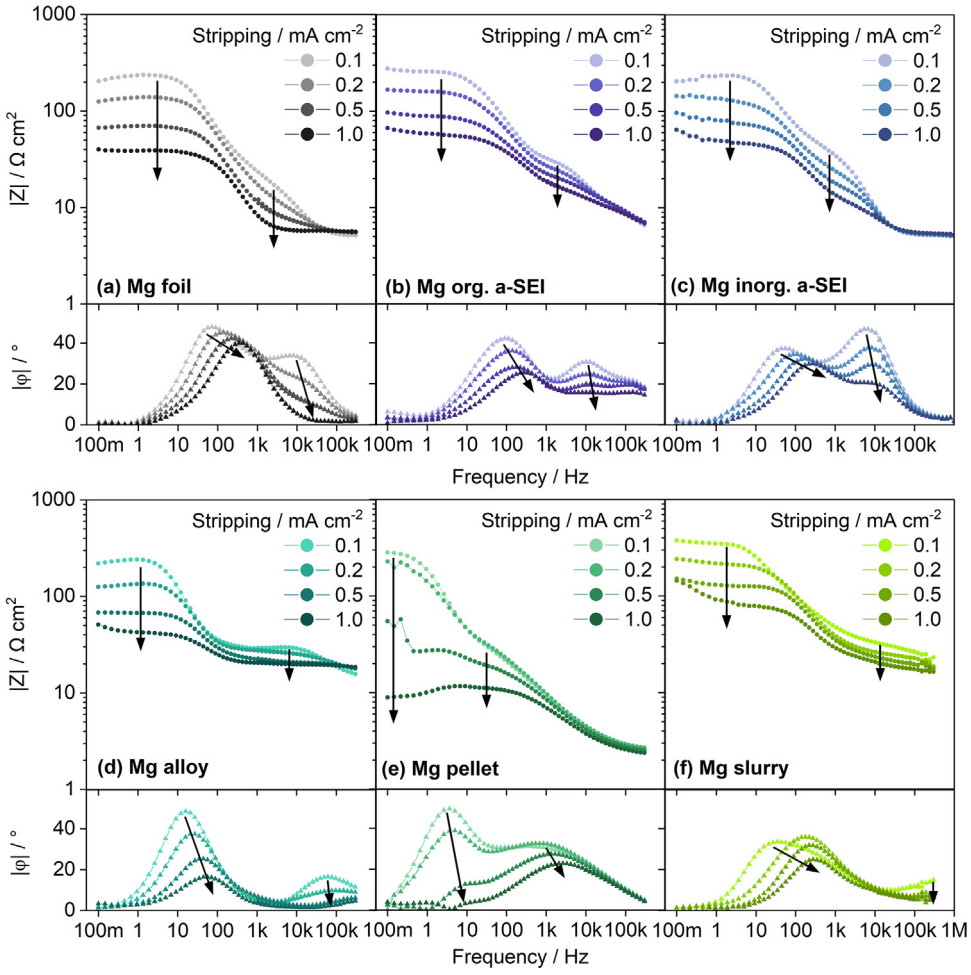

Fig. 6. Bode plots of impedance spectra measured in Mg|Mg cells with different Mg anodes during Mg stripping at different current densities. Polarization at each current density comprised 10 cycles and the spectra were collected at the end of the 10th cycle. Arrows are drawn to indicate the trend in phase angle with increasing current density. (For interpretation of the references to colour in this figure legend, the reader is referred to the web version of this article.)

relevant processes, is prevented. This is of great importance to derive reliable and realistic resistances and recommended for EIS investigation of Mg batteries in general.

3.3.2. Process in the MF region (10 Hz–1 kHz)

Potential processes at a metal electrode surface are the charge transfer (CT) reaction and the migration through the solid electrolyte interphase (SEI)—latter causing an additional diffusion resistance. Previous studies covering EIS of Mg metal in organic electrolytes, assign the MF process to the CT, while the HF process was attributed to the SEI resistance [12,14] and vice versa [44]. Others correlate the observed semicircles in the Nyquist plot with different surface layers [48,49]. To shed light on such contradicting interpretations, the EIS evolution during current variation is investigated herein. As pointed out above, the differences in the impedance spectra of stripping and plating are rather small, thus, the following process assignment only takes the stripping spectra into account (Fig. 6).

Yet both, the corresponding charge transfer resistance R_{ct} and SEI resistance R_{SEI} show the same dependency on the current-density i_0

$$R_{SEI},\ R_{ct} = \frac{RT}{zFi_0} \tag{1}$$

wherein, R, T, z and F are the universal gas constant (8.3145 J mol^{-1}K^{-1}), temperature, number of transferred electrons and Faraday constant (96,485.3 C mol^{-1}), respectively. However, in contrast to the SEI resistance, the accompanied capacitance of the charge transfer, namely the double layer capacitance C_{dl}, remains constant with varying current density as the thickness of the inner Helmholtz layer is determined by the size of the solvent molecules, while the overall electrical double-layer thickness is governed by the Debye length, both of which are independent of the applied current.

$$C_{dl} = \frac{\varepsilon_0 \cdot \varepsilon_r \cdot A}{d_{dl}} = \text{const.} \tag{2}$$

Wherein ε_0, ε_r and A are the dielectric constant of the vacuum (8.8542·10^{-14} F cm^{-1}), dielectric constant of the material and the electrode surface area, respectively. With latter being constant, altering the current-density results in a shift in the characteristic frequency $f_{c,ct}$ of the charge transfer reaction

to higher values.

$$f_{c,ct} = \frac{1}{R_{ct}C_{dl}} \quad (3)$$

The variation of the current density i is therefore a suitable way to identify the charge transfer reaction in an impedance spectrum (Fig. 6). While, according to Eq. (1), the overall impedance decreases with increasing current density, the MF process exhibits a clear shift in its characteristic frequency to higher values (see exemplary f-Im (Z) plot in Fig. S3) and is therefore identified as charge transfer reaction. This is in line with corrosion measurements of Mg metal in aqueous electrolytes [50].

Despite all anodes exhibiting a rather similar overall impedance, the phase angle peaks, an indicator for the characteristic frequency of the interfacial processes, significantly differs. While bare and a-SEI coated Mg metal (Fig. 6a,b,c) have a narrow phase angle peak distribution, the Mg alloy, pellet and slurry (Fig. 6d,e,f) show a large peak separation – with the Mg alloy (Fig. 6d) exhibiting the slowest charge transfer kinetics. An organic a-SEI coating (Fig. 6b) interestingly seems to alter neither the characteristic frequency nor the charge transfer resistance of a Mg metal foil. This indicates thatthere is no mass transport limitation caused by the polymer coating and the kinetics of charge transfer are similar (at least at current densities below 1.0 mA cm^{-2}).

3.3.3. Process in the HF region (1 kHz–1 MHz)

Fig. 7 depicts the impedance and phase angle evolution during polarization at 0.1 mA cm^{-2}. Following the interpretation in the previous section and the extensive study in aqueous media by Wang et al. [51], the remaining process in the HF region (> 1 kHz) is attributed to the SEI resistance.

While the CT process (MF) remains rather constant with ongoing polarization, the SEI process (HF) for all anodes exhibits a decline in both, impedance and phase angle—partially resulting in a negligible contribution after 50 polarization cycles (Fig. 7a,d,f). Assuming the conductivity σ_{SEI} of the SEI (i.e. composition) to be constant, a decline in R_{SEI} implies a decrease in SEI thickness d_{SEI} or increase in surface area A.

$$R_{SEI} = \frac{d_{SEI}}{\sigma_{SEI} \cdot A} \quad (4)$$

Latter is likely, considering the decline in phase angle, which reflects an increase in surface roughness.

Both, organic and inorganic a-SEI coated Mg anodes (Fig. 7b,c) exhibit similar behavior, but still feature an SEI impedance contribution at the end of polarization. This might be caused by different Mg deposition characteristics as a covered Mg surface is more likely to enable uniform plating (resulting in morphologies with low surface area), while a bare magnesium surface is prone to side reactions (resulting in porous deposits with larger surface area) [8].

Generally, the thickness of the SEI is defined by

$$d_{SEI} = \frac{\varepsilon_0 \varepsilon_r A}{C_{SEI}} \quad (5)$$

wherein C_{SEI}, ε_0 and ε_r are the dielectric capacitance of the SEI layer, the permittivity of vacuum ($8.8542 \cdot 10^{-14}$ F cm^{-1}) and the relative permittivity of the SEI components, respectively. According to XPS analysis in our previous studies with the same electrolyte system, an in situ, electrochemically formed SEI consists of MgO and MgF_2 with additionally MgS and potentially $MgSO_4$ in Mg|S cells [1,44]. This SEI composition (Table 1) also holds for the organic SEI due to the in situ SEI formation underneath the organic SEI [1]. As the HF process is already well-defined in the initial spectra, it might also reflect the native oxide layer, i.e. a chemically formed surface layer.

Considering the rather similar dielectric constants, the conductivity of the SEI layer on the Mg alloy and Mg slurry anode (Fig. 7d,f) has to be higher than that on the Mg foil or Mg pellet to result in a higher characteristic frequency (Fig. S4).

$$f_{c,SEI} = \frac{1}{R_{SEI}C_{SEI}} = \frac{\sigma_{SEI}}{\varepsilon_0 \cdot \varepsilon_r} \quad (6)$$

Following first-principle calculations by Canepa et al. [52] the migration barrier of MgO, MgF_2 and MgS is rather high (Table 1). However, as no anode passivation is observed, this does not seem to be detrimental for the ion movement. Thus, the SEI either needs to be very thin or, more likely, be cracked and highly porous to allow direct contact of the electrolyte with the Mg surface. Further elaboration on this is given in the concluding section with equivalent circuit models and derived resistances.

In addition to the HF process (1–50 kHz), the organic a-SEI (Fig. 7b) features an additional process HF' at ultrahigh frequencies (> 50 kHz), which reflects the porous nature of the polymeric coating [1], whereas the pristine anode (Fig. 7a) exhibits only ohmic behavior in this frequency region. This becomes more apparent in the zoomed Nyquist plots wherein the spectra of the org. a-SEI anode exhibits a 45° line in the HF region characteristic for porous media (Fig. S5 and S6). As the polymeric coating is an electrical insulator, no charge transfer occurs within the porous network and the ionic pore resistance can be calculated via following equation.

$$R_{ion} = \frac{\tau \cdot d_{aSEI}}{\varepsilon \cdot A \cdot \sigma_{aSEI}} \quad (7)$$

Therein, τ, $d_{a\text{-}SEI}$, ε and $\sigma_{a\text{-}SEI}$ reflect the tortuosity, thickness, porosity and conductivity of the polymeric coating and A is the geometric surface area of the electrode (2.545 cm^2). Overall, the HF' process exhibits only small changes in impedance and phase angle, reflecting a rather stable artificial SEI layer through the polarization cycles. In contrast, the Mg anode with inorganic a-SEI does not feature an additional HF' process but exhibits similar spectra to bare Mg foil. This reflects its dense, crystalline nature.

3.4. Galvanostatic cycling and EIS analysis of Mg|S cells

3.4.1. Process assignment

To gain further insights in practical cells, galvanostatic cycling of Mg|S cells at C/10 with intermittent EIS measure-

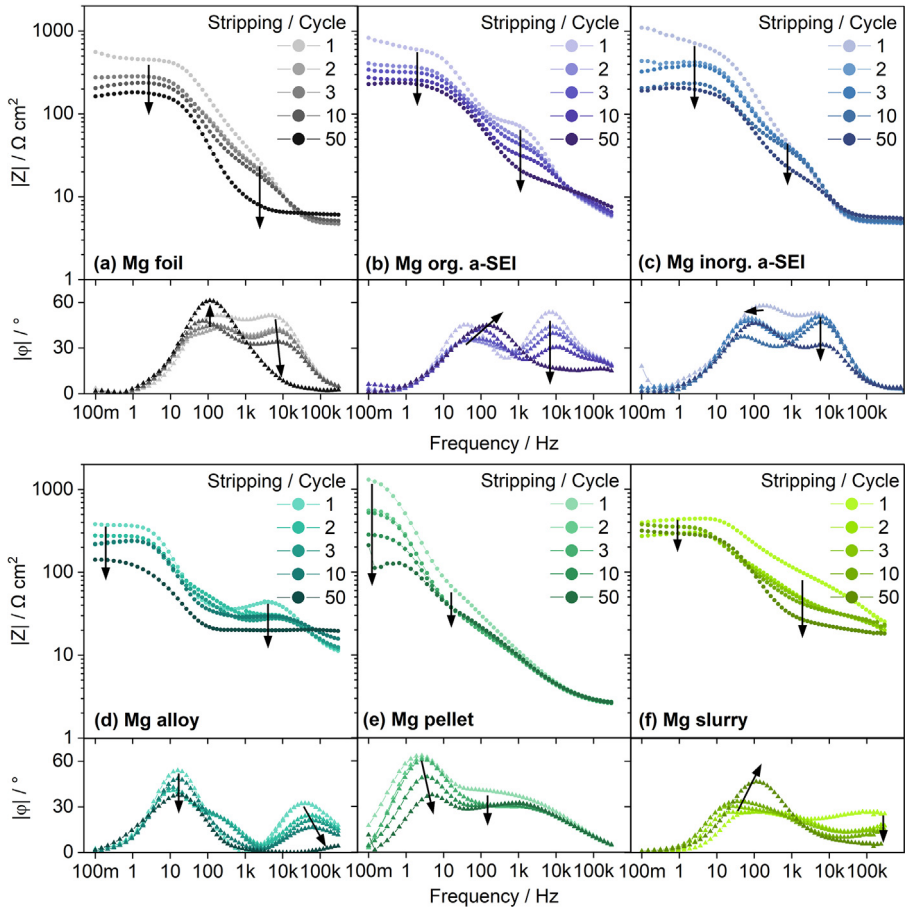

Fig. 7. Bode plots of impedance spectra measured in Mg|Mg cells with different Mg anodes during stripping at 0.1 mA cm^{-2}. Arrows are drawn to indicate the trend in phase angle with time and proceeding polarization. (For interpretation of the references to colour in this figure legend, the reader is referred to the web version of this article.)

Table 1
Relative permittivity and calculated migration barrier of the main SEI components.

Compound	MgO	MgF_2	MgS	$MgSO_4$
ε_r/-	3.2–9.8	2–5 4.87 5.45	6.69	6.2 (x 7 H_2O) 7.36 (x 1 H_2O)
E_m/meV [52]	1851	1123	943	na

ments (vs. Mg-RE) is performed. The voltage profiles of different anodes are depicted in Fig. S7 indicating the benefit of an (organic) artificial SEI to mitigate the reaction of sulfur species at the anode surface. This results in a higher initial voltage after cell assembly, an elongated first discharge plateau and reduced polysulfide shuttle during charging (Fig. S7). As a matter of simplicity and qualitatively similar features, the impedance spectra of bare Mg foil are presented exemplarily in Fig. 8—in both, Bode (a,b) and corresponding Nyquist (c,d) representation.

On first sight, it becomes obvious that discharge, i.e. Mg stripping (Fig. 8a,c) and charge, i.e. Mg plating (Fig. 8b,d) spectra significantly differ, which is in contrast to the symmetrical cells despite the same EIS settings (0.1 mA cm^{-2}, 5 mV amplitude). This is attributed to sulfur species, which diffuse out of the cathode matrix in the electrolyte , to be reduced at the anode surface in parallel to Mg^{2+} ions, while they do not compete during stripping/oxidation [47]. With sulfur and polysulfides contributing to the surface layer formation on the Mg anode, the first charge (Mg plating) significantly alters the Mg surface composition. This becomes evident in the spectra of the subsequent discharge cycles (Fig. 8a, Cycle 2–4), that feature an additional LF process with $f_{c,\,CT}$ = 150–300 mHz (cf. Fig. S8). It is attributed to the charge transfer reaction with sluggish kinetics caused by sulfur contributing to the in situ SEI formation (SEI-2), which is reflected by a rather indistinct MF process ($f_{c,SEI\text{-}2}$ approx. 7 Hz). Interestingly, the charge transfer does not feature such retarded kinetics during charging, i.e. Mg plating (Fig. 8b, Cycle 1–4), with the characteristic frequency of the superimposed CT and in situ SEI-2

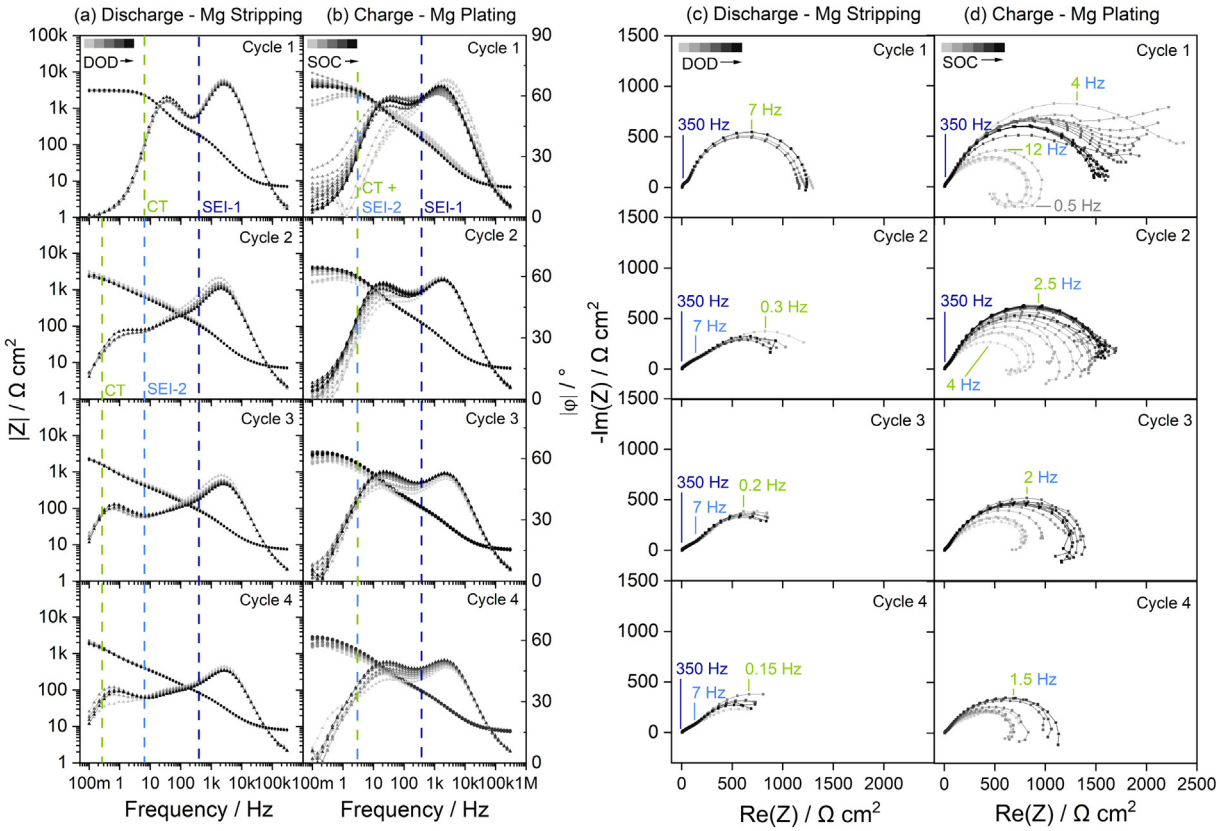

Fig. 8. Evolution of the pristine Mg anode impedance response of Mg|S cells during discharge (Mg stripping) and charge (Mg plating) in Bode (a,b) and Nyquist representation (c,d). The specific characteristic frequencies are indicated. Cycling with C/10 rate (0.167 mA cm^{-2}), galvanostatic ("dynamic") EIS at 0.1 mA cm^{-2} with 5 mV amplitude. ● |Z| (left axis), ▲ |φ| (right axis).

only shifting from initial 12 Hz to 1.5 Hz. This is assigned to a surface layers breakage during Mg plating with the freshly deposited Mg not exhibiting the retarded kinetics as during stripping wherein the layers withstand the volume changes.

Despite showing a benefit in capacity and coulombic efficiency, the artificial SEI (Fig. S9) is not capable to mitigate the parasitic reactions during charge, and thus rather similar spectra in terms of impedance and phase angle result. In contrast to the bare Mg foil, the SEI-2 process is less significant due to mitigated diffusion of sulfur species towards the Mg surface. In comparison to the symmetrical cell, the organic a-SEI contribution in the ultrahigh frequency region is more pronounced with a distinct straight line during initial discharge (Fig. S10). Interestingly, the contribution is reduced during charge but rebuilds in the subsequent cycles.

The inorganic a-SEI (Fig. S11) shows similar features with the MF process splitting into two distinguishable contributions ($f_{c,SEI-2}$ = 9 Hz, $f_{c,CT}$ = 0.45 Hz) after the first charge (Mg plating). In contrast, the HF process becomes faster by one order of magnitude ($f_{c,SEI-1}$ = 500 Hz to 5 kHz) and less pronounced. The Mg slurry anode (Fig. S11) interestingly does not feature any HF process (SEI-1) after some cycles and the CT is actually faster than that of the other anodes ($f_{c,CT}$ = 2 Hz) reflecting the benefit of the increased Mg surface area.

3.4.2. Origin of inductive loops

Apparently, the Nyquist charge spectra at low SOC are dominated by low frequency hooks, often named inductive loops (Fig. 8d, Fig. S9, S11, S12). Interestingly, in Mg|Mg cells, such loops appear in both, Mg plating and stripping (Fig. 9a,b), while they are only visible upon stripping in Mg|S cells. It is aimed to shed light on the origin of this phenomenon below.

Generally, the loop appearance can either be linked to a surface process on Mg metal, or arises from a RE misalignment or its geometrical/electrochemical asymmetry towards the working electrode. Herein, the latter can be ruled out as such loops also appear in impedance spectra of 2E cells applying magnesium foils (Fig. 9c). However, no inductive loops are present, when using Mg pellets – neither as WE/CE in a 2E cell (Fig. 9d) nor as RE in a 3E cell (Fig. 9e, Fig. S13), which is linked to its higher surface area and/or conditioned surface with a native oxide layer (no prior scraping).

In general, a reference electrode should provide a stable and reliable potential with negligible voltage drift (few mV) over time. Furthermore, it should be non-polarizable by small currents (originated in potentiostat electronics or cell's leakage resistance) [53] and exhibit a high impedance. As EIS artifacts can arise due to electrochemical and geometrical asymmetry, a ring shape is most recommended [54,55]. Latter is

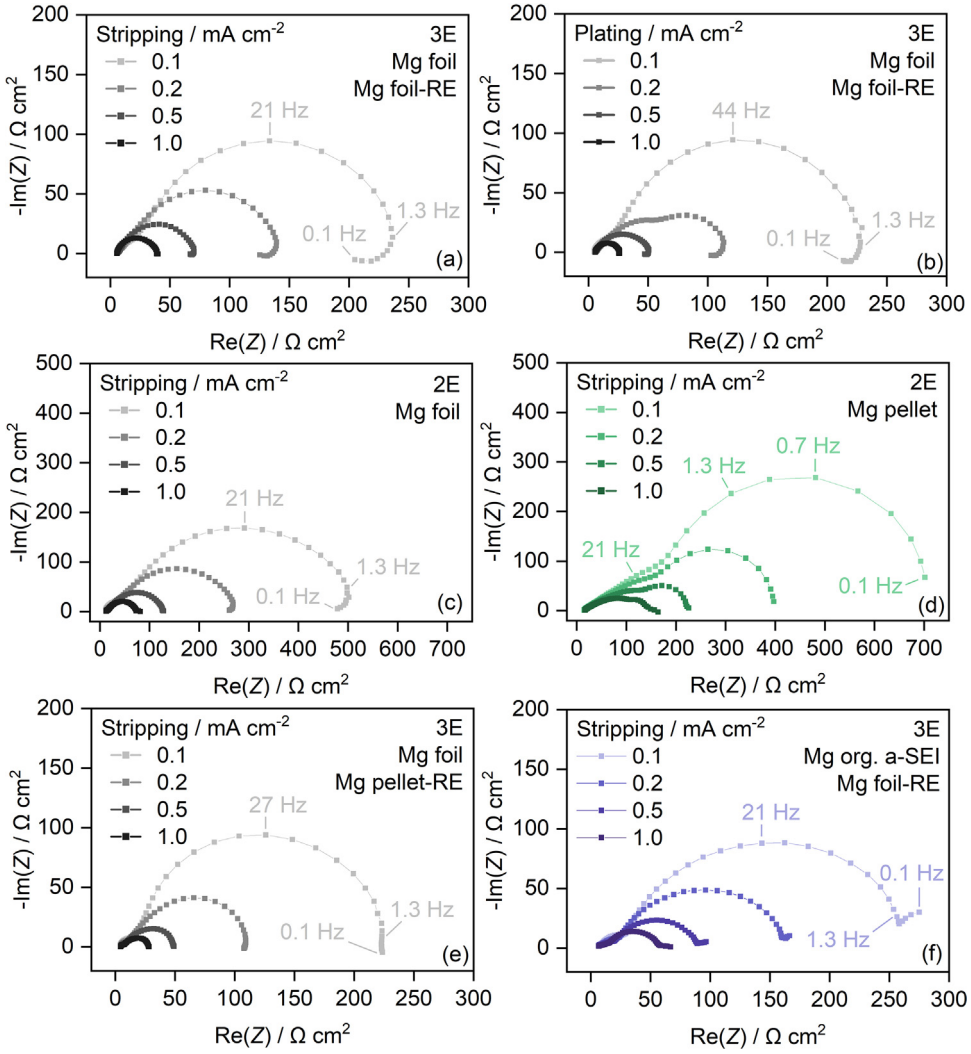

Fig. 9. Present/absent inductive loops in Nyquist plots from a (a,b) Mg foil 3E cell with Mg foil-RE, (c) Mg foil 2E cell, (d) Mg pellet 2E cell, (e) Mg foil 3E cell with Mg pellet-RE, (f) Mg org. a-SEI 3E cell with Mg foil-RE, at different current densities.

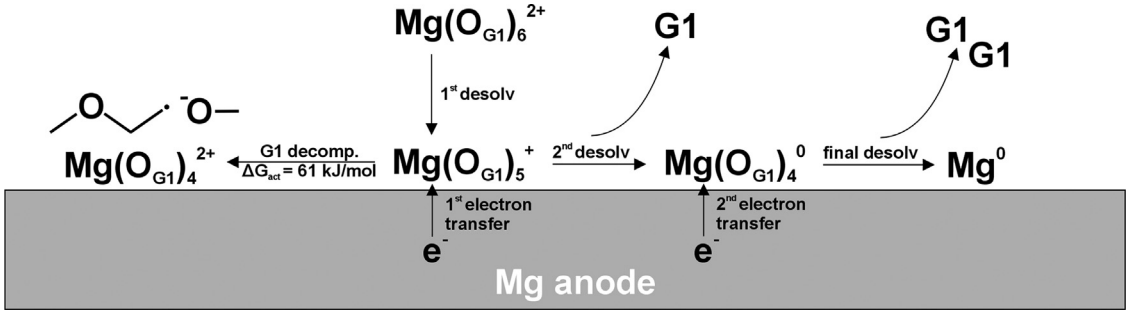

Fig. 10. Mg plating mechanism according to DFT calculations [9,66]. O_{G1} refers to an G1 oxygen atom coordinated to the Mg cation (2 per G1 molecule). Anions are not considered due to the low ion pair ratio (low salt concentration and bulky anion in general). Apart from the plating route, also solvent decomposition might occur. (For interpretation of the references to colour in this figure legend, the reader is referred to the web version of this article.)

ensured herein by applying a Mg metal ring—either cut from Mg metal foil or pressed from Mg powder (Mg pellet-RE). It was observed, that while the foil-RE does not exhibit a constant relaxation potential during polarization (Fig. S14a), i.e. the surface is not in an equilibrium state, the pellet-RE in contrast features a rather stable OCV potential, which remains constant in subsequent polarization. After the first polarization cycle, the potentials of the pellet and foil reference electrode are identical pointing to an activated Mg foil surface (Fig. S14a). This is in agreement with previous studies, in which

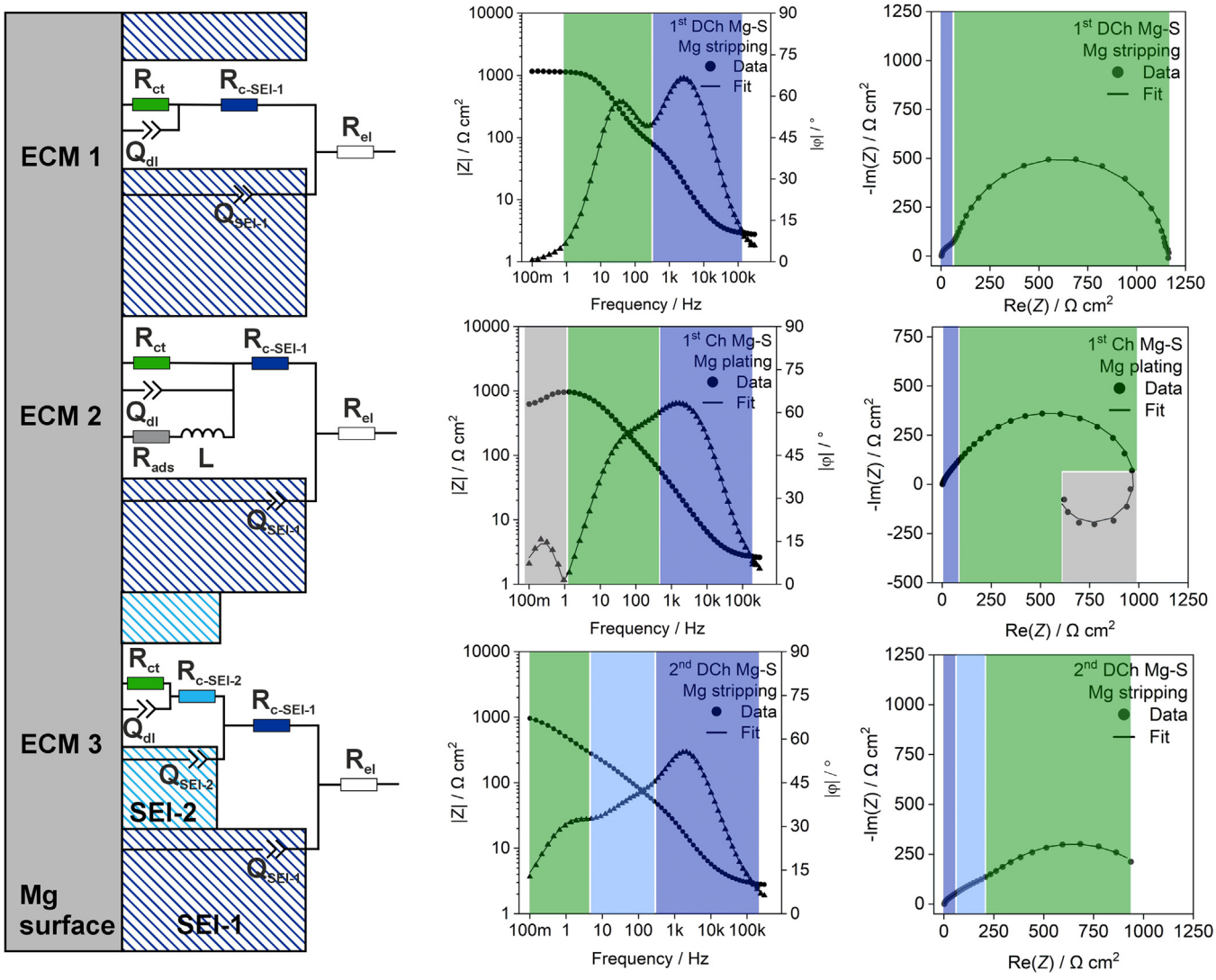

Fig. 11. Proposed equivalent circuit models (ECM) applicable for Mg anodes with inorganic SEI layers: Mg foil, inorganic a-SEI, Mg alloy and Mg pellet. The interfacial processes are depicted in exemplary Bode and Nyquist plots for bare Mg foil during cycling in a Mg|S cells. Bode plot: • |Z| (left axis), ▲ |φ| (right axis).

multivalent metals like Mg (in contrast to Li metal) were found to be unsuitable due to the RE surface being altered in contact with electrolyte [53,54]. This is presumed to be triggered by stronger ion-solvent interactions, sluggish mass transport and a low cation transference number derived from the divalent ion character [56]. Therefore we suggest the Mg pellet-RE as a convenient and reliable alternative.

Apart from the RE, a surface coating on the planar magnesium foil also alters the impedance response. With an organic a-SEI, the anode spectra in Mg|Mg cells mostly feature no loops, but a semicircle branch in the low-frequency region (Fig. 9f). Generally, the inductive loops appear to be current-dependent and attenuate or even vanish at high current densities (Fig. 9c). The influence of an increasing surface area with proceeding polarization of the Mg foil can be neglected as the loops are present even in the 50th cycle at 0.1 mA cm^{-2} (Fig. S15).

The inductive loops are confirmed to be a physical surface process at planar, unconditioned magnesium metal—yet its distinct origin is difficult to assign. Indeed, such loops are previously observed in various reports about EIS of magnesium in aqueous media with their interpretations being well summarized by Wang et al. [51] Based on our observations herein as well as the existing literature we conclude the plausible origin of the inductive loop in EIS response of Mg cells as follows (Table 2).

To elaborate on this and narrow down the origin, the Mg plating mechanism in Mg[B(hfip)$_4$]$_2$/G1 electrolytes proposed by DFT calculations [9,66] in (Fig. 10, right route) is discussed. Therein, O_{G1} denotes G1 oxygen ligands with three G1 molecules fully coordinating the Mg^{2+} cation (CN = 6). After an initial rate-determining desolvation and the fast subsequent first electron transfer, a $Mg(O_{G1})_5^{+}$ intermediate results. As the monovalent Mg ion is highly reactive, it might

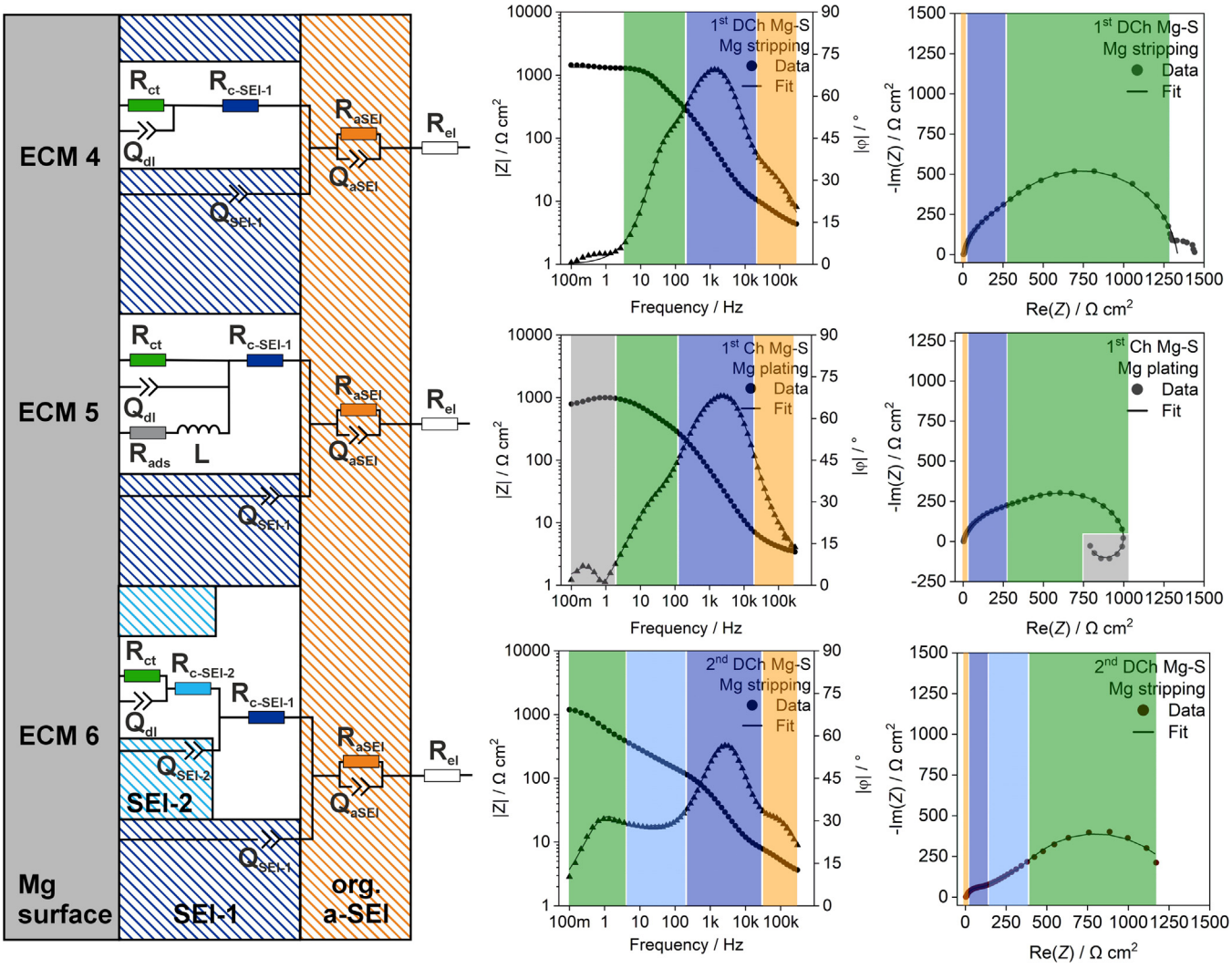

Fig. 12. Proposed equivalent circuit models (ECM) applicable for Mg anodes with a porous, organic SEI in addition to the inorganic SEI: organic a-SEI and Mg slurry. The interfacial processes are depicted in exemplary Bode and Nyquist plots for the organic a-SEI anode during cycling in a Mg|S cells. Bode plot: • |Z| (left axis), ▲ |φ| (right axis).

Table 2
Aspects influencing the inductive loop formation and the potential origin at the Mg metal surface reported in literature.

	Aspects	Potential origin
Mg|Mg	- Appears during Mg stripping and plating - Vanishes with increasing current - Vanishes with surface coating or alloy - Less dominant with high surface area	- Relaxation [57–60] or Desorption [52] of an adsorbed intermediate (Mg^{+}_{ads}) - Breakdown of a surface film (oxidation products like $Mg(OH)_2$) [34,35,61–63]
Mg|S	- Only appears during charging (Mg plating) - Dominant at low charge SOC - Sulfur species competing in Mg reduction	- Nucleation of local corrosion [64] or an increased corrosion rate (no Mg^{+}) [65]

either be further reduced to Mg^0 after a second desolvation, or reoxidized by transferring the electron to a G1 molecule, i.e. decomposing it [66]. In either case, the lifetime and surface diffusion of $Mg(O_{G1})_5^{+}$ is supposed to be limited. Nevertheless, surface relaxation of the adsorbed intermediates will occur to a certain extent. However, this does not solely explain the dominant appearance during the initial charge SOC. Therein, localized corrosion, which even result in macroscopic holes within the Mg electrode after cycling [1], might indeed be the origin. This is linked to salt or solvent decomposition (cf. Fig. 10, left route), or uneven stripping [37]. Overall, the inductive loops might be caused by both processes, diffusion of adsorbed intermediates and localized corrosion.

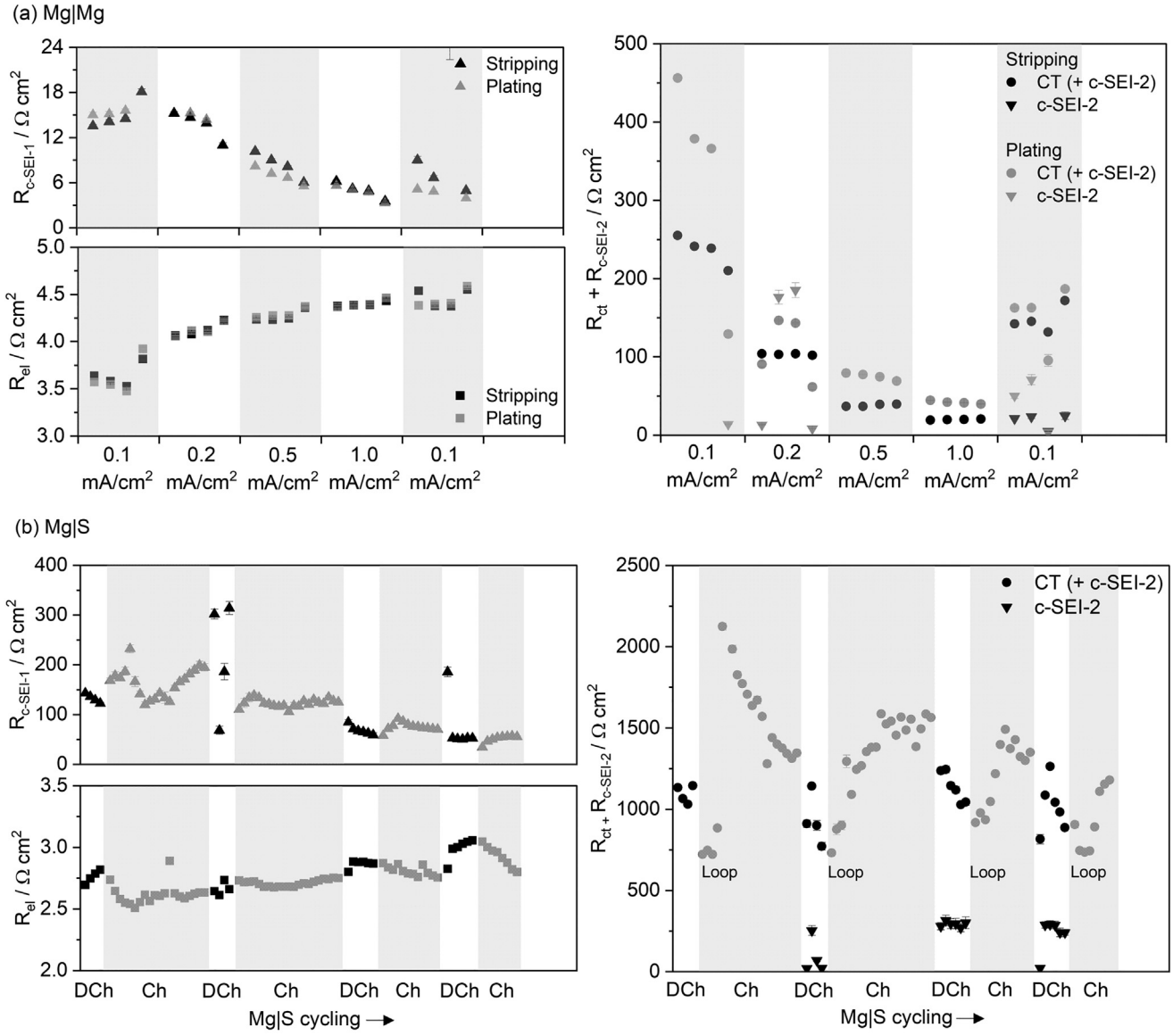

Fig. 13. Resistance evolution at bare Mg foil as anode in (a) Mg|Mg and (b) Mg|S cells. Due to the above-mentioned spectra variations, ECM1–3 are applied for fitting, resulting in the partially distinguishable resistance $R_{c\text{-}SEI\text{-}2}$.

3.4.3. Equivalent circuit models

Based on the gained insights and process assignments in Mg|Mg and Mg|S cells, it was attempted to derive general equivalent circuit models (ECM), which include the identified processes and are applicable to all anode approaches. Due to above named spectra deviations, the anode approaches are devided into two main groups—anodes with an inorganic SEI (Mg foil, inorganic a-SEI, Mg alloy and Mg pellet, Fig. 11) and anodes with an additional porous, organic SEI (organic a-SEI and Mg slurry, Fig. 12). Latter includes an additional R-CPE, which reflects the HF' process, i.e. diffusion through the tortuous polymeric a-SEI coating.

Generally, the inorganic surface layers (denoted SEI) are assumed to be porous and cracked (indicated by an indexed "c" in the resistances) to allow sufficient Mg^{2+} transport. Therefore, the SEI resistances will most probably be related to the liquid phase, yet the solid conduction pathways or their influence could not be fully excluded, so it is good to consider this as a hybrid system. They are further divided into contributions from a mainly chemically formed, native SEI, $R_{c\text{-}SEI\text{-}1}$ (mainly MgO and specifically the inorg. a-SEI) and an electrochemically formed SEI, $R_{c\text{-}SEI\text{-}2}$ (mainly MgF_2 and MgS).

The ordinary ECM 1 and 4, which follows L. Wang et al. [51], assume a charge transfer at the bare Mg surface without surface relaxation and are applicable to spectra of Mg|Mg cells with inorganic and organic SEI, respectively. While those spectra mostly allow the use of the same ECM throughout the polarization, the Mg|S cells require several ECM during cycling due to significant changes in the initial cycles, e.g. the inductive loop during charging (cf. Fig. 8d). This is usually represented by an inductor (L)—like in the corresponding

ECM 2 established by Boukamp et al. [67]—but it actually lacks direct physical interpretation as inductive effects occur in the HF region (induced by cables). Others applied such ECM already in Mg-air batteries [34,68] and Mg corrosion studies [60–62]. Klotz demonstrated by ECM conversion [69] that such "LF hook" can also be modelled by a series of RC circuits applying negative resistance and capacitance values [70]. This indeed has also no physical meaning but neither does the exponent α in constant phase elements (CPE), which is widely accepted. As this controversy is beyond the scope of this manuscript, the most common ECM is applied (ECM 2 and 5).

During the second and subsequent Mg stripping (discharge) in Mg|S cells an additional LF semicircle is present, which is represented in ECM 3 and 6 by another R-CPE circuit [71]. Interestingly, similar behavior is observed during Mg plating in Mg|Mg cells (Fig. 5). As discussed above, this is assigned to the retarded charge transfer kinetics—most probably due to a less ion-conductive and probably cracked in situ SEI layer ($R_{c\text{-}SEI\text{-}2}$), which becomes distinguishable in the MF region of the impedance spectra. This observation is also reported by Wang et al. for aqueous Mg batteries [50]. Note again, that $R_{c\text{-}SEI\text{-}2}$ is most likely also present in other spectra, yet not distinguishable due to exhibiting a similar characteristic frequency as the charge transfer and therefore being superimposed.

3.4.4. Influence of sulfur species

The resulting resistances from the ECM fitting were exemplary depicted in Fig. 13 for bare Mg foil. In Mg|Mg cells (Fig. 13a), $R_{c\text{-}SEI\text{-}1}$ is declining with increasing current density to almost become negligible—and remains constant when again applying a low current density. This reflects the mainly native SEI to be cracked over a large surface area. This is backed by the estimation of its conductivity and thickness in the initial stages of polarization/cycling reflecting a significantly higher conductivity (1E-8 S cm^{-1}) than MgO (< 1E-14 S cm^{-1}), see Supplementary Material, Table S2. Simultanously, the electrolyte resistance R_{el} is slightly increasing, indicating an ongoing in situ SEI formation to consume the electrolyte. The charge transfer resistance R_{ct} (+ $R_{c\text{-}SEI\text{-}2}$) also declines with current density, but in contrast to $R_{c\text{-}SEI\text{-}1}$ reversibly exhibits larger resistances when again applying a low current density. The deviation between the initial and final polarization at 0.1 mA cm^{-2} most likely arises from an increased surface area. The charge transfer resistance during plating is slightly higher than during stripping, $R_{c\text{-}SEI\text{-}1}$ and R_{el} do not vary with stripping/plating.

Comparing the anode resistances gained from Mg|Mg and Mg|S cells (Fig. 13b), the influence of sulfur species becomes obvious. The overall charge transfer resistance is significantly higher and exhibits an undulatory trend, i.e. decrease during discharge (Mg stripping) and increase during charging (Mg plating). This reflects the sulfur species to compete with Mg^{2+} reduction and their contribution to the in situ SEI formation. In contrast to the rather stable $R_{c\text{-}SEI\text{-}2}$ (Fig. 13b) the resistance $R_{c\text{-}SEI\text{-}1}$ assigned to the chemically formed SEI features

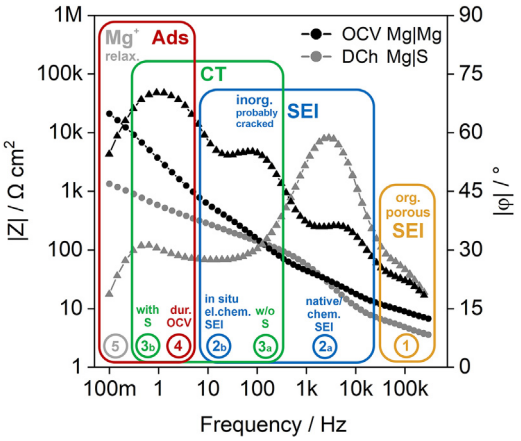

Fig. 14. Exemplary bode plot of a Mg anode impedance (● |Z| (left axis), ▲ |φ| (right axis)) summarizing the assigned interfacial processes occurring at the Mg anode surface during OCV/cycling and with/without sulfur species in its vicinity.

a declining trend—similar to the Mg|Mg cell, but with lower conductivity (8E-11 vs. 1E-8 S cm^{-1}, Table S2) probably due to MgS formation. This trend is reproducible and steady with ongoing polarization/cycling—and independent from the artificial SEI (Fig. S16).

Interestingly, the sulfur species also influence the formation of the high-ohmic adsorption layer in the LF region during rest at OCV. While it forms instantly in symmetrical cells, its evolution is mitigated to some extent in Mg|S cells (Figure S17). As investigated in an operando UV/Vis spectroscopy study, even during non-current conditions, dissolved sulfur species diffuse to the anode and react at its surface to form polysulfides or sulfide/sulfate surface layers leading to a higher c-SEI-1 resistance in comparison to the Mg|Mg cell [43]. These ongoing reactions might hinder the solvent and salt molecules from adsorbing at the Mg surface. Further, considering the Bode plots (Fig. S18), the SEI and CT process are already distinguishable in Mg|S cells after cell assembly, with latter building up during 1 h OCV.

4. Conclusion

The present study depicts and discusses the advantages and drawbacks of different Mg anode approaches as well as their similarities and differences in terms of interfacial processes during Mg|Mg polarization and Mg|S cycling. Therefore, electrochemical impedance spectroscopy was applied and a systematic process assignment was performed. Due to changes during cell operation, different ECM were proposed including the plausible processes in such systems summarized in Fig. 14. The native, probably cracked inorganic SEI layer (2a) is observed within every approach, while the organic artificial SEI (1) reveals its porous nature with an additional process in the HF region. The occurrence and characteristic of the other interfacial processes strongly depends on the SOC during cycling and the presence of sulfur species, which affect

the plating/reduction process and the surface layer formation. The in situ SEI (2b) is only partially distinguishable from the charge transfer in symmetrical cells and during discharge of Mg|S cells (Mg stripping). The charge transfer ($Mg \leftrightarrow Mg^{2+}$) exhibits retarded kinetics in the presence of sulfur species (3b) with the overall impedance and time constant being significantly increased in comparison to sulfur-free cells (3a). The high-ohmic adsorption layer (4) forms reversibly during non-current conditions independent of the applied anode, but has no relevance during cell operation as the adsorbed electrolyte species instantly desorb when applying a current. In Mg|S cells, its formation competes with the non-faradaic sulfur reduction, i.e. self-discharge, and consequential surface layer formation. Due it partially overlapping with other processes, operando EIS is crucial for conducting a reliable EIS analysis. In the LF region, inductive loops (5) appear during Mg plating, especially during charging of Mg|S cells, which most likely reflects a surface relaxation of adsorbed monovalent magnesium ions.

All anode approaches exhibit a current-dependent stripping/plating overpotential asymmetry, which related to the rate limiting step of Mg^{2+} desolvation during plating. Among all anodes, the organic a-SEI possesses the lowest asymmetry, i.e. facilitated desolvation, yet on the expense of an additional diffusion resistance. Interestingly, despite the significant plating/stripping asymmetry, the impedance spectra hardly differ between stripping and plating, which indicates the desolvation of Mg^{2+} ions to have less influence on the interfacial processes visible in EIS measurements. The Mg pellet and Mg slurry approach do potentially offer the benefit of an increased surface area, yet due to native oxide layers, the surface is only partially active—and they are no practical option due to the large thickness and dead voids. However, a thin aluminum mesh to function as current collector into which Mg particles are pressed by a rolling procedure might be an interesting future approach as the Mg excess can then be minimized without losing the current collector scaffold (Fig. 14).

The suitability of the other approaches is apparently linked to the active mass loading of the cathode, which defines the balanced anode thickness. While Mg foil and the Mg alloy AZ31 might be most promising for high-loadings (anode thickness > 30 μm) and cost-effective processing, the PVD approach is well-suited to tailor the Mg excess while giving the advantage to simultaneously introduce an inorganic artificial SEI layer.

Generally, the study indicates options to tailor the interfacial processes of different Mg anodes to further enhance their electrochemical performance toward practical and competitive Mg batteries. Despite derived with focus on Mg-S batteries, the findings are expected to be at least qualitatively transferable to other systems like magnesium-air batteries.

Declaration of competing interests

The authors declare that there is no conflict of interests regarding the publication of this article.

CRediT authorship contribution statement

Joachim Häcker: Writing – review & editing, Writing – original draft, Visualization, Project administration, Methodology, Investigation, Funding acquisition, Formal analysis, Data curation, Conceptualization. **Tobias Rommel:** Writing – review & editing, Investigation, Formal analysis, Data curation. **Pia Lange:** Writing – review & editing, Investigation, Formal analysis. **Felix Kampmann:** Writing – review & editing, Resources. **Jürgen Remmlinger:** Writing – review & editing, Resources, Project administration, Funding acquisition. **Zhirong Zhao-Karger:** Writing – review & editing, Resources. **K. Andreas Friedrich:** Supervision, Project administration, Funding acquisition. **Maryam Nojabaee:** Writing – review & editing, Validation, Supervision, Project administration, Funding acquisition.

Acknowledgements

This work is financially supported by the Federal Ministry for Education and Research of Germany (Bundesministerium für Bildung und Forschung, BMBF) and the European Commission within the projects “MagSiMal” (03XP0208) and “E-MAGIC” (824066), respectively. The authors express their gratitude to Aleksey Kovalevsky (Technion - Israel Institute of Technology, Israel) for providing thin AZ31 sheets, Giulia Bonfanti and Ina Plock (DLR Stuttgart, Germany) for SEM sample preparation and characterization, as well as Norbert Wagner (DLR Stuttgart, Germany) and Matthias Hahn (EL-Cell GmbH, Germany) for the various fruitful discussions about EIS and reference electrodes.

Supplementary materials

Supplementary material associated with this article can be found, in the online version, at doi:10.1016/j.jma.2025.04.001. It provides EDX analysis, additional voltage profiles and impedance spectra as well as an exemplary estimation of the SEI thickness/conductivity and f-Im(Z) plots to derive the characteristic frequency.

References

[1] J. Häcker, T. Rommel, P. Lange, Z. Zhao-Karger, T. Morawietz, I. Biswas, N. Wagner, M. Nojabaee, K.A. Friedrich, ACS Appl. Mater. Interfaces 15 (27) (2023) 33013–33027, doi:10.1021/acsami.3c07223.
[2] P. Bonnick, J. Muldoon, Adv. Funct. Mater. 30 (21) (2020) 1910510, doi:10.1002/adfm.201910510.
[3] Z. Zhao-Karger, E.G. Bardaji, O. Fuhr, M. Fichtner, J. Mater. Chem. A 5 (22) (2017), doi:10.1039/C7TA02237A.
[4] Z. Zhao-Karger, R. Liu, W. Dai, Z. Li, T. Diemant, B.P. Vinayan, C. Bonatto Minella, X. Yu, A. Manthiram, R.J. Behm, et al., ACS Energy Lett. 3 (8) (2018) 2005–2013, doi:10.1021/acsenergylett.8b01061.
[5] S.C. Bevilacqua, K.H. Pham, K.A. See, Inorg. Chem. 58 (16) (2019) 10472–10482, doi:10.1021/acs.inorgchem.9b00891.
[6] G. Bieker, J. Wellmann, M. Kolek, K. Jalkanen, M. Winter, P. Bieker, Phys. Chem. Chem. Phys 19 (2017) 11152–11162, doi:10.1039/C7CP01238A.
[7] G.T. Cheek, W.E. O’Grady, S.Z. El Abedin, E.M. Moustafa, F. Endres, J. Electrochem. Soc. 155 (1) (2008) D91, doi:10.1149/1.2804763.

[8] B. Dlugatch, M. Mohankumar, R. Attias, B.M. Krishna, Y. Elias, Y. Gofer, D. Zitoun, D. Aurbach, ACS Appl. Mater. Interfaces 13 (46) (2021) 54894–54905, doi:10.1021/acsami.1c13419.

[9] J. Drews, P. Jankowski, J. Hacker, Z. Li, T. Danner, J.M. Garcia Lastra, T. Vegge, N. Wagner, K.A. Friedrich, Z. Zhao-Karger, et al., ChemSusChem 14 (21) (2021) 4820–4835, doi:10.1002/cssc.202101498.

[10] J. Lowe, D.J. Siegel, J. Phys. Chem. C 122 (20) (2018) 10714–10724, doi:10.1021/acs.jpcc.8b01752.

[11] F. Sagane, K. Ogi, A. Konno, K. Kanamura, J. Electrochem. Soc. 166 (3) (2018) A5054–A5058.

[12] V. Bhaghavathi Parambath, Z. Zhao-Karger, T. Diemant, M. Jäckle, Z. Li, T. Scherer, A. Gross, R.J. Behm, M. Fichtner, J. Mater. Chem. A 8 (43) (2020) 22998–23010, doi:10.1039/d0ta05762b.

[13] H. Kurihara, M. Inamoto, H. Ogasa, Chem. Lett. 50 (6) (2021) 1213–1216, doi:10.1246/cl.210072.

[14] X. Li, T. Gao, F. Han, Z. Ma, X. Fan, S. Hou, N. Eidson, W. Li, C. Wang, Adv. Energy Mater. 8 (2018) 1701728, doi:10.1002/aenm.201701728.

[15] Z. Li, T. Diemant, Z. Meng, Y. Xiu, A. Reupert, L. Wang, M. Fichtner, Z. Zhao-Karger, ACS Appl. Mater. Interfaces 13 (28) (2021) 33123–33132, doi:10.1021/acsami.1c08476.

[16] Z. Meng, Z. Li, L. Wang, T. Diemant, D. Bosubabu, Y. Tang, R. Berthelot, Z. Zhao-Karger, M. Fichtner, ACS Appl. Mater. Interfaces 13 (31) (2021) 37044–37051, doi:10.1021/acsami.1c07648.

[17] J. Zhang, X. Guan, R. Lv, D. Wang, P. Liu, J. Luo, Energy Storage Mater. 26 (2020) 408–413, doi:10.1016/j.ensm.2019.11.012.

[18] F. Liu, G. Cao, J. Ban, H. Lei, Y. Zhang, G. Shao, A. Zhou, L.z. Fan, J. Hu, J. Magnes. Alloys 10 (10) (2022) 2699–2716, doi:10.1016/j.jma.2022.09.004.

[19] H. Xu, T. Xie, Y. Li, F. Sun, C. Zhang, Z. Li, Y. Yao, Y. Li, Y. Zhan, X. Zou, et al., Adv. Energy Mater. 14 (33) (2024) 2401154, doi:10.1002/aenm.202401154.

[20] Y.Y. Hwang, N.K. Lee, S.H. Park, J. Shin, Y.J. Lee, Energy Storage Mater. 51 (2022) 108–121, doi:10.1016/j.ensm.2022.06.014.

[21] J. Xu, Z. Wei, P. Chen, W. Yan, T. Li, C. Chen, Mater. Lett. 287 (2021) 12925, doi:10.1016/j.matlet.2020.129253.

[22] T. Mandai, H. Somekawa, Batter. Supercaps 5 (2022) e202200153, doi:10.1002/batt.202200153.

[23] B. Li, R. Masse, C. Liu, Y. Hu, W. Li, G. Zhang, G. Cao, Energy Storage Mater. 22 (2019) 96–104, doi:10.1016/j.ensm.2019.06.035.

[24] E. Sahadeo, G. Rubloff, S.B. Lee, C.-F. Lin, Front. Energy Res. 9 (2021) 618368, doi:10.3389/fenrg.2021.618368.

[25] H. Wang, J. Ryu, S.A. McClary, D.M. Long, M. Zhou, M.H. Engelhard, L. Zou, J. Quinn, P. Kotula, K.S. Han, et al., J. Electrochem. Soc. 168 (12) (2021) 120519, doi:10.1149/1945-7111/ac3d2c.

[26] R. Zhang, C. Cui, R. Xiao, L. Ruinan, T. Mu, H. Huo, Y. Ma, G. Yin, P. Zuo, Chem. Eng. J. 444 (2022) 136592, doi:10.1016/j.cej.2022.136592.

[27] C. Pechberty, A. Hagopian, J.-B. Ledeuil, D. Foix, J. Allouche, J.-N. Chotard, O. Lužanin, J. Bitenc, R. Dominko, R. Dedryvère, et al., J. Mater. Chem. A 10 (22) (2022) 12104–12113, doi:10.1039/d2ta02083a.

[28] J. Touja, N. Louvain, L. Stievano, L. Monconduit, R. Berthelot, Batter. Supercaps 4 (8) (2021) 1252–1266, doi:10.1002/batt.202100009.

[29] R. Li, Q. Liu, R. Zhang, Y. Li, Y. Ma, H. Huo, Y. Gao, P. Zuo, J. Wang, G. Yin, Energy Storage Mater. 50 (2022) 380–386, doi:10.1016/j.ensm.2022.05.039.

[30] Z. Meng, D. Foix, N. Brun, re Dedryv\'e, mi R\'e, L. Stievano, M. Morcrette, R. Berthelot, ACS Energy Lett. 4 (9) (2019) 2040–2044.

[31] J. Niu, Z. Zhang, D. Aurbach, Adv. Energy Mater. 10 (23) (2020) 2000697, doi:10.1002/aenm.202000697.

[32] T. Tsukeda, M. Moriwaki, T. Nakagawa, T. Aida, H. Tabata, H. Kurihara, M. Suzuki, J. Jpn. Soc. Exp. Mech. 22 (1) (2022) 15–19, doi:10.11395/jjsem.22.15.

[33] S. Vincent, J.H. Chang, J.M. Garcia Lastra, Batter. Supercaps 4 (3) (2020) 522–528, doi:10.1002/batt.202000240.

[34] N. Wang, W. Li, Y. Huang, G. Wu, M. Hu, G. Li, Z. Shi, J. Power Sources 436 (2019) 226855, doi:10.1016/j.jpowsour.2019.226855.

[35] H. Xiong, K. Yu, X. Yin, Y. Dai, Y. Yan, H. Zhu, J. Alloys Compd. 708 (2017) 652–661, doi:10.1016/j.jallcom.2016.12.172.

[36] A. Maddegalla, A. Mukherjee, J.A. Blazquez, E. Azaceta, O. Leonet, A.R. Mainar, A. Kovalevsky, D. Sharon, J.F. Martin, D. Sotta, et al., ChemSusChem 14 (21) (2021) 4690–4696, doi:10.1002/cssc.202101323.

[37] X. Liu, A. Du, Z. Guo, C. Wang, X. Zhou, J. Zhao, F. Sun, S. Dong, G. Cui, Adv Mater 34 (31) (2022) e2201886, doi:10.1002/adma.202201886.

[38] T. Wen, H. Xiao, S. Tan, X. Huang, B. Qu, L. Cao, G. Huang, J. Song, J. Wang, A. Tang, et al., J. Magnes. Alloys 12 (7) (2024) 2647–2673, doi:10.1016/j.jma.2024.04.010.

[39] B. Sievert, J. Häcker, F. Bienen, N. Wagner, K.A. Friedrich, ECS Trans. 77 (11) (2017) 413, doi:10.1149/07711.0413ecst.

[40] S.-B. Son, T. Gao, S.P. Harvey, K.X. Steirer, A. Stokes, A. Norman, C. Wang, A. Cresce, K. Xu, C. Ban, Nat. Chem. 10 (5) (2018) 532–539, doi:10.1038/s41557-018-0019-6.

[41] J. Liu, H. Hu, T. Wu, J. Chen, X. Yang, N. Wang, Z. Shi, J. Magnes. Alloys 12 (4) (2024) 1554–1565, doi:10.1016/j.jma.2022.07.016.

[42] W. Wang, S. Luo, L. Mo, S. Guo, Q. Cai, X. Yang, Z. Shi, N. Wang, J. Power Sources 624 (2024) 235579, doi:10.1016/j.jpowsour.2024.235579.

[43] J. Häcker, D.H. Nguyen, T. Rommel, Z. Zhao-Karger, N. Wagner, K.A. Friedrich, ACS Energy Lett. 7 (2022) 1–9, doi:10.1021/acsenergylett.1c02152.

[44] J. Häcker, C. Danner, B. Sievert, I. Biswas, Z. Zhao-Karger, N. Wagner, K.A. Friedrich, Electrochim. Acta 338 (2020) 135787, doi:10.1016/j.electacta.2020.135787.

[45] J. Wang, R. Yu, J. Wang, J. Long, F. Qiao, L. Zhang, G. He, Q. An, L. Mai, J. Magnes. Alloys 11 (11) (2023) 4181–4188, doi:10.1016/j.jma.2023.10.001.

[46] O. Tutusaus, R. Mohtadi, N. Singh, T.S. Arthur, F. Mizuno, ACS Energy Lett. 2 (1) (2017) 224–229.

[47] T. Gao, S. Hou, K. Huynh, F. Wang, N. Eidson, X. Fan, F. Han, C. Luo, M. Mao, X. Li, et al., ACS Appl. Mater. Interfaces 10 (17) (2018) 14767–14776, doi:10.1021/acsami.8b02425.

[48] B.P. Vinayan, H. Euchner, Z. Zhao-Karger, M.A. Cambaz, Z. Li, T. Diemant, R.J. Behm, A. Gross, M. Fichtner, J. Mater. Chem. A 7 (44) (2019) 25490–25502, doi:10.1039/C9TA09155F.

[49] F.A.L. Laskowski, S.H. Stradley, M.D. Qian, K.A. See, ACS Appl Mater Interfaces 13 (25) (2021) 29461–29470, doi:10.1021/acsami.1c02788.

[50] L. Wang, D. Snihirova, M. Deng, B. Vaghefinazari, D. Höche, S.V. Lamaka, M.L. Zheludkevich, Electrochim. Acta 404 (2021) 139582, doi:10.1016/j.electacta.2021.139582.

[51] L. Wang, D. Snihirova, M. Deng, C. Wang, B. Vaghefinazari, G. Wiese, M. Langridge, D. Höche, S.V. Lamaka, M.L. Zheludkevich, Corros. Sci. 187 (2021) 109501, doi:10.1016/j.corsci.2021.109501.

[52] T. Chen, G. Sai Gautam, P. Canepa, Chem. Mater. 31 (19) (2019) 8087–8099, doi:10.1021/acs.chemmater.9b02692.

[53] R. Dugas, J.D. Forero-Saboya, A. Ponrouch, Chem Mater 31 (21) (2019) 8613–8628, doi:10.1021/acs.chemmater.9b02776.

[54] S. Klink, E. Madej, E. Ventosa, A. Lindner, W. Schuhmann, F.L. Mantia, Electrochem. Commun. 22 (2012) 120–123, doi:10.1021/acsami.6b06190.

[55] J. Costard, M. Ender, M. Weiss, E. Ivers-Tiffée, J. Electrochem. Soc. 164 (2) (2017) A80–A87, doi:10.1149/2.0241702jes.

[56] D.S. Tchitchekova, D. Monti, P. Johansson, F. Bardé, A. Randon-Vitanova, M.R. Palacín, A. Ponrouch, J. Electrochem. Soc. 164 (7) (2017) A1384–A1392, doi:10.1149/2.0411707jes.

[57] M.P. Gomes, I. Costa, N. Pébère, J.L. Rossi, B. Tribollet, V. Vivier, Electrochim. Acta 306 (2019) 61–70, doi:10.1016/j.electacta.2019.03.080.

[58] G. Baril, G. Galicia, C. Deslouis, N. Pébère, B. Tribollet, V. Vivier, J. Electrochem. Soc. 154 (2) (2007) C108–C113. doi:10.1149/1.2401056

[59] S. Leleu, B. Rives, J. Bour, N. Causse, N. Pébère, Electrochim. Acta 290 (2018) 586–594, doi:10.1016/j.electacta.2018.08.093.

[60] X. Wang, Z. Chen, J. Ren, H. Kang, E. Guo, J. Li, T. Wang, Corros. Sci. 164 (2020) 108318, doi:10.1016/j.corsci.2019.108318.
[61] T. Zhang, G. Meng, Y. Shao, Z. Cui, F. Wang, Corros. Sci. 53 (9) (2011) 2934–2942, doi:10.1016/j.corsci.2011.05.035.
[62] X. Chen, Q. Zou, Q. Le, J. Hou, R. Guo, H. Wang, C. Hu, L. Bao, T. Wang, D. Zhao, et al., J. Power Sources 451 (2020) 227807, doi:10.1016/j.jpowsour.2020.227807.
[63] S. Yin, W. Duan, W. Liu, L. Wu, J. Yu, Z. Zhao, M. Liu, P. Wang, J. Cui, Z. Zhang, Corros. Sci. 166 (2020) 108419, doi:10.1016/j.corsci.2019.108419.
[64] I. Nakatsugawa, R. Martin, E.J. Knystautas, Corros. Sci. 52 (12) (1996) 921.
[65] V. Shkirskiy, A.D. King, O. Gharbi, P. Volovitch, J.R. Scully, K. Ogle, N. Birbilis, Chemphyschem 16 (3) (2015) 536–539, doi:10.1002/cphc.201402666.
[66] P. Jankowski, Z. Li, Z. Zhao-Karger, T. Diemant, M. Fichtner, T. Vegge, J.M.G. Lastra, Energy Storage Mater. 45 (2022) 1133–1143, doi:10.1016/j.ensm.2021.11.012.
[67] B.A. Boukamp, B.A. Van Hassel, I.C. Vinke, K.J. De Vries, A.J. Burggraaf, Electrochim. Acta 38 (14) (1993) 1817–1825.
[68] X. Liu, S. Liu, J. Xue, J. Power Sources 396 (2018) 667–674, doi:10.1016/j.jpowsour.2018.06.085.
[69] S. Fletcher, *J. Electrochem. Soc.*, **141** (7), 1994, 1823.
[70] D. Klotz, Electrochem. Commun. 98 (2019) 58–62, doi:10.1016/j.elecom.2018.11.017.
[71] M.E. Orazem, B. Tribollet, Electrochemical Impedance Spectroscopy, in: Chapter 9: Equivalent Circuit Analogs, John Wiley & Sons, Inc, Hoboken, New Jersey, 2008, pp. 158–161.